# The Hybrid Recharge Delayed Oscillator: A More Realistic El Niño Conceptual Model

TAKESHI IZUMO, a,b MAXIME COLIN, c,d FEI-FEI JIN, e AND BASTIEN PAGLI

(Manuscript received 6 March 2023, in final form 19 January 2024, accepted 29 January 2024)

ABSTRACT: El Niño-Southern Oscillation (ENSO) is the leading mode of climate interannual variability, with large socioeconomical and environmental impacts, potentially increasing with climate change. Improving its understanding may shed further light on its predictability. Here we revisit the two main conceptual models for explaining ENSO cyclic nature, namely, the recharge oscillator (RO) and the advective-reflective delayed oscillator (DO). Some previous studies have argued that these two models capture similar physical processes. Yet, we show here that they actually capture two distinct roles of ocean wave dynamics in ENSO's temperature tendency equation, using observations, reanalyses, and Climate Model Intercomparison Project (CMIP) models. The slow recharge/discharge process mostly influences central-eastern Pacific by favoring warmer equatorial undercurrent and equatorial upwelling, while the 6-month delayed advective-reflective feedback process dominates in the western-central Pacific. We thus propose a hybrid recharge delayed oscillator (RDO) that combines these two distinct processes into one conceptual model, more realistic than the RO or DO alone. The RDO eigenvalues (frequency and growth rate) are highly sensitive to the relative strengths of the recharge/discharge and delayed negative feedbacks, which have distinct dependencies to mean state. Combining these two feedbacks explains most of ENSO frequency diversity among models. Thanks to the two different spatial patterns involved, the RDO can even capture ENSO spatiotemporal diversity and complexity. We also develop a fully nonlinear and seasonal RDO, even more robust and realistic, investigating each nonlinear term. The great RDO sensitivity may explain the observed and simulated richness in ENSO's characteristics and predictability.

SIGNIFICANCE STATEMENT: El Niño and La Niña events, and the related Southern Oscillation, cause the largest year-to-year variations of Earth's climate. Yet the theories behind them are still debated, with two main conceptual models being the recharge oscillator and the delayed oscillator. Our purpose here is to address this debate by developing a more realistic theory, a hybrid recharge delayed oscillator. We show how simple yet realistic it is, with equivalent contributions from the slow recharge process and from the faster delayed feedback. It even captures the observed El Niño and La Niña diversity in space and in frequency. Future studies could use the simple theoretical framework provided here to investigate El Niño–Southern Oscillation (ENSO) in observations, theories, climate models diagnostics and forecasts, and global warming projections.

KEYWORDS: El Nino; Ocean dynamics; ENSO; Seasonal forecasting; Interannual variability; Tropical variability

#### 1. Introduction

El Niño-Southern Oscillation (ENSO) is the leading mode of climate interannual variability, with large socioeconomical and environmental impacts, and with its extremes possibly increasing with global warming (e.g. Cai et al. 2021). The basic ENSO amplification dynamics has been fairly well understood

© Supplemental information related to this paper is available at the Journals Online website: https://doi.org/10.1175/JCLI-D-23-0127.s1.

Colin's current affiliation: Leibniz Centre for Tropical Marine Research (ZMT), Bremen, Germany.

Corresponding author: Takeshi Izumo, takeshi.izumo@ird.fr

(e.g. Neelin et al. 1998; Wang and Picaut 2004; Clarke 2008 reviews). Yet there are still debates on the main mechanisms at play for ENSO phase reversal and its related quasi-cyclic nature, on ENSO theories/conceptual models (e.g. Graham et al. 2015; Santoso et al. 2017; Timmermann et al. 2018; Jin et al. 2020), and on how to implement ENSO diversity in these conceptual models (Fang and Mu 2018; Geng et al. 2020; Chen et al. 2022; Thual and Dewitte 2023). ENSO diversity, a continuum from extreme eastern Pacific (EP) El Niño events to western-central Pacific (CP) El Niño Modoki (e.g. Trenberth and Stepaniak 2001; Ashok et al. 2007; Takahashi et al. 2011; Capotondi et al. 2015, 2020), and even encompassing La Niña events (Monselesan et al. 2023, submitted to J. Climate), is crucial to understand/forecast ENSO global impacts (e.g. Johnson and Kosaka 2016), e.g. on tropical cyclones activity in the Pacific, notably over vast French Polynesia (Vincent et al. 2011; B. Pagli et al., unpublished manuscript).

DOI: 10.1175/JCLI-D-23-0127.1

ENSO events usually initiate in boreal spring, develop in summer and autumn and then decay in the next spring (e.g. Bunge and Clarke 2009; Fang and Zheng 2021). They develop because of the Bjerknes positive feedback. Positive sea surface temperature (SST) anomalies in the central-eastern equatorial Pacific  $(T_E)$  enhance deep atmospheric convection in the central Pacific, resulting in westerly wind stress anomalies in the westerncentral Pacific ( $\tau_x$ ; Clarke 1994). These in turn force equatorial downwelling Kelvin waves with eastward surface currents that advect the warm pool eastern edge eastward (e.g. Picaut et al. 1996; Vialard et al. 2001) and thermocline depth (h) positive anomalies towards the central-eastern equatorial Pacific, thereby reinforcing the initial SST anomalies. This positive feedback mechanism is offset by several negative instantaneous and delayed feedbacks. The delayed negative feedbacks result from oceanic dynamics: 1) a slow negative feedback related to the wind-driven slower equatorial basin adjustment to El Niño westerlies that acts to create a discharge (and a recharge in the La Niña easterlies case) of warm water volume (WWV)/oceanic heat content (OHC, proportional to h; e.g. Jin 1997a,b; Meinen and McPhaden 2000; Clarke 2010; Zhu et al. 2017; Izumo et al. 2019; Izumo and Colin 2022) of the southwestern and equatorial Pacific (Fig. 1b), 2) a rapid ~6-month delayed advective-reflective feedback through equatorial oceanic wave reflections (e.g. Boulanger and Menkes 2001; Boulanger et al. 2004; cf. Fig. 1a and section 3).

Two main groups of theories have emerged to explain the quasi-cyclic nature of ENSO, based on the aforementioned negative oceanic feedbacks: 1) the recharge oscillator (RO; e.g. Wyrtki 1985; Jin 1997a,b; Meinen and McPhaden 2000; Clarke et al. 2007; Clarke 2010; Thual et al. 2013), 2) the delayed oscillator (Suarez and Schopf 1988; Battisti and Hirst 1989) and its improved version emphasizing the crucial role of Indo-Pacific warm pool eastern edge, the advective–reflective delayed oscillator (DO; Picaut et al. 1997). An in-depth description of the RO and DO is given in section 3. Other conceptual models, e.g. the unified oscillator (Wang 2001), have been shown to be less realistic (Graham et al. 2015).

Some studies question the RO and suggest that the DO is more realistic (e.g. Linz et al. 2014; Graham et al. 2015). Yet, the recharge/discharge process is also part of ENSO cycle, both in observations and models. One reason for this "RO vs DO" debate is that RO and DO have been seen as two different formal ways to represent the same wave adjustment process favoring an ENSO phase reversal (e.g. Jin 1997a,b; Jin and An 1999). But actually, they mainly involve different physical processes with different timescales (Fig. 1). For the RO, it is the slow ( $\sim$ 1–2 years) equatorial basin adjustment (e.g. Izumo et al. 2019, their Fig. S4) influencing central-eastern Pacific SST through the thermocline feedback (e.g. Wyrtki 1985; Jin 1997a,b), and through oceanic heat transport changes (Izumo 2005; Ballester et al. 2015, 2016). For the DO, it is the faster (~6-month) equatorial wave reflection influencing central Pacific SST through the zonal advective feedback (Vialard et al. 2001). So, is it really fair to consider the RO and DO as a single mechanism while they capture distinct physical processes and have different impacts on the  $T_E$  tendency equation?

Here we show, by analyzing observations/reanalyses (section 4b) and 79 Coupled Model Intercomparison Project (CMIP) models (section 4c), that we should keep both the recharge and advective-reflective delayed feedbacks as two distinct crucial processes in the ENSO temperature tendency equation, without considering them as formally identical. By keeping both of them, we obtain a more physically based and more realistic ENSO conceptual model, a hybrid recharge delayed oscillator (RDO; schematics in Fig. 1; derivation of its equations in section 4a). We then analyze the behavior of this RDO. Section 4d explores the eigenvalues dependency to parameters, within the observations and CMIP parameter space. Section 4e first investigates the RDO response to stochastic forcing and related spectral response. It then shows how ENSO characteristics (amplitude and spectrum) in the RDO framework are highly sensitive to the relative strengths of the recharge and delayed negative feedback. Section 4f shows that the RDO can, even its simplest form, capture some ENSO spatiotemporal diversity, if we take into account the spatial dependency of these feedbacks. Section 5 then improves the simplest RDO framework, by adding 1) the seasonal cycles of RDO parameters (section 5a) and 2) asymmetries/nonlinearities, e.g., quadratic terms and a multiplicative noise (section 5b). Section 5 confirms the robustness of the RDO framework, with the nonlinear seasonal RDO version being even more realistic than the linear RDO version. Finally, section 6 summarizes the results and discusses mechanisms, possible improvements of the RDO, implications, and perspectives.

#### 2. Data and methods

See Text S1 in the online supplemental material for a detailed description of the typical statistical methods we use, plus additional details on data, indices, and validation/sensitivity tests. Note that for the nonlinear seasonal version of the RDO (section 5), the scripts for obtaining the RDO parameters through multivariate linear regression fits and for running the RDO forced by red noise were developed in Python language within the framework of the RO community model under development as a follow-up of the RO review by J. Vialard et al. (unpublished manuscript).

#### a. Data

For SST observations we use the following monthly datasets: Optimum Interpolation SST OISSTv2 based on in situ observations and satellite measurements for the recent period (November 1981–March 2022; Reynolds et al. 2002; hereafter "obs1"); HadiSSTv1.1 SST (1870–March 2022; Rayner et al. 2003) when using longer-time-scale reanalyses. We also use GPCP monthly precipitation (Adler et al. 2003) for developing the approximated formula of sensitivity of precipitation to relative SST.

We use SLA as a proxy for thermocline depth (e.g. 20°C isotherm depth, Z20) and oceanic heat content (OHC) anomalies (e.g. Rebert et al. 1985; Gasparin and Roemmich 2017; Palanisamy et al. 2015; see Izumo and Colin 2022 for a detailed comparison of SLA, Z20, and OHC for the recharge index). SLA is advantageous because it has been measured since three decades by satellites (Copernicus product; 1993–mid 2021;

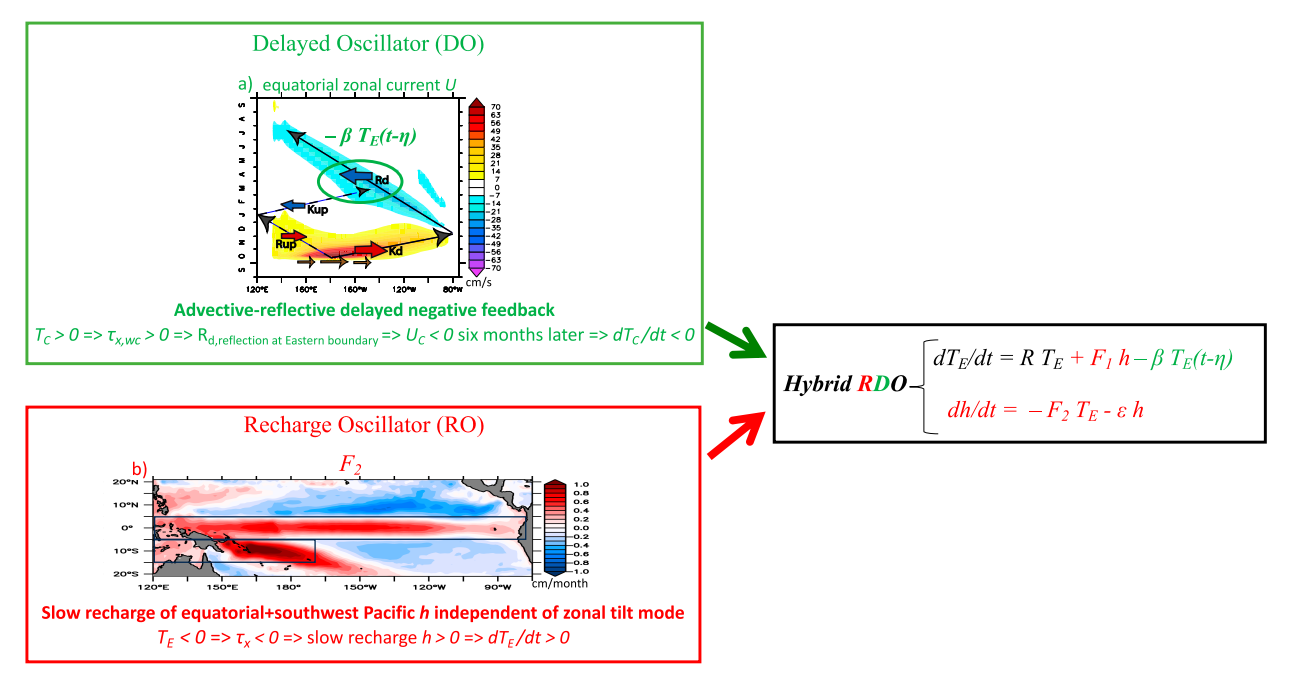


FIG. 1. Schematics of the recharge delayed oscillator (RDO) principle, combining (top left) the advective–reflective delayed oscillator (DO; green; representing mainly the zonal feedback; Picaut et al. 1997) and (bottom left) the recharge oscillator (RO; red; representing the slow recharge process; Jin 1997a,b). (top left) Equatorial zonal current response (in the upper-oceanic layer, color shading and red and blue arrows) to a westerly pulse in early October in the western-central Pacific (brown arrows), with equatorial waves (black arrows for downwelling waves, dashed arrows for upwelling waves) and their reflections indicated schematically [in particular the downwelling Kelvin wave  $K_d$  with positive zonal current reflecting at the eastern boundary as a downwelling Rossby wave  $R_d$  with opposite negative current; see Izumo et al. (2016) for details on a similar idealized pulse experiment starting in January]. (bottom left) Slow recharge of  $h_{\text{ind}}$  (SLA independent of the fast zonal tilt mode) forced by La Niña easterly anomalies (i.e. the  $-F_2T_E$  term obtained by multivariate regression in obs1; vice versa for a discharge during El Niño).  $T_C$  and  $U_C$  denote central equatorial Pacific SST and zonal current, respectively;  $T_E$  denotes central-eastern Pacific SST; h is the objectively optimized recharge index developed in Izumo and Colin (2022) [(bottom left) here adapted from Fig. 2h of their study], i.e. SLA (or Z20) averaged over the equatorial and southwest Pacific [black boxes in the bottom left], namely,  $h_{\text{ind}}|_{\text{eq+sw}}$  ( $h_{\text{ind}}|_{\text{eq+sw}}$ ); note that the RDO robustness does not depend much of the recharge index choice; cf. section 2).

"obs1"), allowing a homogeneous spatiotemporal sampling. We also use longer SLA datasets for comparison and to increase the number of effective degrees of freedom: ECMWF ORAS5 oceanic reanalysis extended version [1959-2018; Zuo et al. 2019; hereafter "obs2"; we also use its subsurface potential temperature and currents (currents only available from 1975)]; even longer SLA from a historical oceanic reanalysis, SODA2.2.6 (1871-2008; Giese and Ray 2011; without subsurface assimilation to avoid spurious trends; hereafter 'hist'), required to estimate the nonlinear seasonal version of the RDO, for which the number of parameters to fit strongly increases (section 5). We subtract from the SLA its 60°S-60°N global average at each time step to remove sea level rise global trend due to global warming, and we also remove any additional regional trend through a linear regression.

A total of 32 CMIP5 and 47 CMIP6 (CMIP phases 5 and 6; Table S1) models are analyzed here. They are the ones for which we have SST and SLA available, for the historical runs (usually 1861–2005 for CMIP5 and 1850–2015 for CMIP6). This amounts to more than 10 000 years of model data to test the validity of our hypotheses.

#### b. ENSO indices

For the ENSO index,  $T_E$ , we use the usual Niño-3.4 region (5°N-5°S, 170°-120°W), where the main ENSO SST variability is located in observations. We define  $T_E$  as Niño-3.4 relative SST (RSST, i.e. SST minus its 20°N-20°S tropical mean; Vecchi and Soden 2007), as recommended by Izumo et al. (2020) and van Oldenborgh et al. (2021) because atmospheric tropical deep convection interannual anomalies are rather related to RSST than to SST, notably under external forcing, i.e. anthropogenic (see also Johnson and Xie 2010; Johnson and Kosaka 2016; Williams and Patricola 2018; Okumura 2019) or volcanic forcing (Khodri et al. 2017; Izumo et al. 2018). The deep convection threshold SST  $> \sim 27^{\circ}$ –28°C (e.g. Gadgil et al. 1984) translates into RSST  $> \sim 1$ °C, a threshold that remains valid with global warming (e.g. Johnson and Xie 2010). See Text S3 of Izumo and Colin (2022) for an extensive discussion justifying the relevance of RSST for ENSO and RO equations. Note that using SST instead of RSST gives quasi-similar results. But it is safer to use RSST because of external forcing.  $T_E$  is normalized by its standard deviation (STD).

For the recharge index (see details and sensitivity tests in Text S1), there has been a debate on which recharge index best measures the slow recharge/discharge process: which averaging region [e.g. western Pacific (120°E-155°W) or whole equatorial band (120°E-80°W)  $h_w$  or  $h_{eq}$  in 5°N-5°S] and which variable [SLA, Z20 (i.e. warm water volume WWV) or OHC] should we use (e.g. Meinen and McPhaden 2000; Planton et al. 2018; Izumo et al. 2019)? Izumo and Colin (2022) have thus developed a physically unambiguous and objectively optimized index of the ENSO slow recharge mode, out of phase with  $T_E$  (i.e. uncorrelated to  $T_E$  at lag 0 and "independent" of the fast adjustment zonal tilt mode, by regressing out from h its component linearly related to  $T_E$  approximately considered to be this fast tilt mode). Here we thus use their optimal improved index  $h_{\text{ind\_eq+sw}}$ : the SLA averaged over the equatorial plus southwestern Pacific [eq + sw box: equatorial box (5°N-5°S, 120°E-80°W) + southwest box (5°-15°S, 120°E-170°W)], from which  $T_E$  variability has been regressed out, to build a recharge index statistically independent from  $T_E$ . In other words,  $h_{ind\_eq+sw} =$  $h_{\rm eq+sw} - KT_E \approx h_{\rm eq+sw}$  (as regression coefficient K is small thanks to the addition of the southwest Pacific region to the equatorial band for the recharge index, e.g. 0.30 for obs2, if all indices are normalized, i.e., shared variance between  $h_{\rm eq+sw}$ and  $T_E$  only of 9%). Its advantage is that it is "orthogonal" to  $T_E$ , so it is a pure additional degree of freedom capturing the slow recharge, without being polluted by the fast tilt mode. Also, its approximation  $h_{eq+sw}$  is simple and easy to compute.

Anyway, we would like to emphasize that the RDO robustness does not depend a lot on the recharge index choice. The RDO implementation would still be useful and robust if one were using usual indices (e.g.  $h_{\rm eq}$  or  $h_w$ ) with the  $\beta$ ,  $F_1$ , and  $F_2$  terms still highly significant (cf. section 4). Furthermore, both  $\beta$  and the final correlation skill of  $dT_E/dt$  tendency equation, (6), will be mathematically exactly the same whether or not we remove the dependent component of h index, as  $T_E$  is also one of the other variables of the multivariate regression. Therefore, if the users have a preference, they can also use the typical  $h_{\rm eq}$  or  $h_w$  indices for the implementation of RDO. Only the overall skill of the RDO equations to represent observed temperature and recharge tendencies will be weaker than if  $h_{\rm ind\_eq+sw}$  or  $h_{\rm eq+sw}$  is used. For the sake of simplicity and clarity of the equations, the optimal recharge index  $h_{\rm ind\_eq+sw}$  will be hereafter noted as "h".

## 3. The two main simple ENSO conceptual models: the RO and the DO

## a. The recharge oscillator

The recharge oscillator (RO) theory (Jin 1997a,b) focuses on the slow oceanic negative feedback on SST associated with wind-driven equatorial OHC variations (Meinen and McPhaden 2000), as aforementioned. It brings long oceanic memory across ENSO phases. During La Niña, easterlies favor a slow recharge of OHC (i.e., a deepening of the thermocline depth *h*) in the equatorial and southwestern Pacific (Fig. 1b). The El Niño event will in turn lead to a discharge favoring a reversal to La Niña conditions, and so on.

The RO equations (Jin et al. 2020; Izumo and Colin 2022) are

$$dT_E/dt = R_{RO}T_E + F_{1,RO}h, (1)$$

$$dh/dt = -F_2 T_E - \varepsilon h, \tag{2}$$

where  $R_{\rm RO}$  is the net effect of Bjerknes positive feedback and instantaneous negative feedbacks,  $F_{1\_{\rm RO}}$  the recharge/discharge influence on  $T_E$ ,  $F_2$  the slow recharge/discharge forced by La Niña/El Niño, and  $\varepsilon$  a Newtonian damping on h. The subscript RO is added to avoid ambiguity when necessary.

Using the improved optimal recharge index "h" =  $h_{\rm ind\_eq+sw}$ , independent of  $T_E$  (cf. section 2),  $\varepsilon$  is negligible in observations and in all CMIP models (Fig. 4b; see section 4b). Therefore, we neglect it at first for the simplest RDO framework (linear and without seasonal cycle). This RO system of two differential equations has the form of a harmonic oscillator (Jin 1997a).

## b. The delayed oscillator (DO)

The zonal advective-reflective delayed oscillator (DO) is based on the relatively rapid equatorial wave reflections causing a 4- to 8-month delayed negative feedback dominated by the zonal advective term (Picaut et al. 1997; Vialard et al. 2001) in the central Pacific where the coupling with atmospheric deep convection is the largest. For example, El Niño westerlies force an equatorial downwelling Kelvin wave  $K_{d,\text{forced}}$  (i.e. equatorial zonal current anomaly U' > 0 and eastward displacement of the warm pool eastern edge) reflecting at the eastern boundary into a downwelling Rossby wave  $R_{d,reflection}$  (i.e. U' < 0) bringing back the edge westward half a year later (Fig. 1a) (there is also a  $R_{\rm up,forced}$ forced to the west of the westerly anomaly, propagating westward and reflecting at the western boundary as an eastward  $K_{\text{up,reflection}}$ wave; e.g. Boulanger and Menkes 2001). This strong zonal advective delayed feedback favoring ENSO phase reversal is well observed, simulated, and understood. Formally, it relates zonal current interannual anomalies to the evolution of zonal wind stress anomalies  $\tau_x$  over the preceding months. The equatorial Pacific Ocean dynamics being quasi-linear (at intraseasonal to interannual timescales), the response to any wind stress anomaly  $\tau_r(t)$  with a typical ENSO wind pattern is the convolution of this  $\tau_x(t)$  to the linear oceanic impulse response. Thus, the anomalies can be approximated as a "causal" filter of  $\tau_x$ :  $\tau_{x,Am}(t-t_1) - c\tau_{x,Bm}(t-t_2)$ , where  $t_1$  is  $\sim 0$ –2 months, the difference  $t_2 - t_1$  is  $\sim 4$ –6 months, where the subscript (e.g., Am) stands for a A-month running mean and c varies depending on  $\tau'_{r}$  anomaly location, and of the variable (U, SLA, or SST; cf. Izumo et al. 2016). For  $U_C$  anomalies, they are approximately proportional to the zonal wind stress anomalies 1-2 months earlier minus a fraction of the wind stress anomalies 7-8 months earlier. The first term represents the fast oceanic response, while the second one represents the delayed negative feedback associated with wave reflection at both boundaries. A realistic approximation of  $U_C$  is

$$U_C(t) \approx A[\tau_x(t) - \beta_0 \tau_x(t - \eta)], \tag{3}$$

where  $\tau_x$  is equatorial zonal wind stress, A is a constant, and  $\beta_0$  is e.g.  $\sim$ 2/3 for  $U_C$  at 0°N, 170°W [based on Table 1 of Izumo et al. (2016) combined with the approximation  $\tau_{x,2m} \approx \tau_{x,1m}$  valid for periods longer than intraseasonal]. We consider the delay  $\eta$  to be approximately 6 months for the sake of simplicity, as it is

rather well constrained by equatorial wave propagation times in a fixed basin geometry, with the main mode (first baroclinic mode) celerity well known in the equatorial Pacific. This formula is an excellent approximation of the response of the quasi-linear continuously stratified equatorial Pacific Ocean (with a realistic coastline) to a wind stress forcing with an ENSO-like spatial pattern. It is more realistic than previous approximations of  $U_C$  used in previous RO-based conceptual models.

We can combine (3) with some typical assumptions to derive a DO equation for  $T_C$ , where  $T_C$  is the SST anomaly in the central equatorial Pacific. We suppose: 1)  $\tau_x \approx \mu_C T_C$  ( $\mu_C$  being a coupling parameter), 2) the zonal SST gradient in the central Pacific to be its climatological value (i.e. independent of the anomaly  $T_C$ ) at first order ( $dT_C/dx \approx dT_{C\_clim}/dx \approx -C$ , with C > 0; hence the zonal advection term is  $CU_C$ ; relaxing this assumption leads to nonlinear terms such as in section 5), and 3) that atmospheric fluxes can be approximated as a weak Newtonian damping (term  $-r_{\text{damp}}T_C$ ), weaker than the Bjerknes feedback related to the first term in the above equation for  $U_C$ . Thus, we have, using (3):

$$\begin{split} dT_C/dt &\approx -U_C(t)dT_C/dx(t) - r_{\rm damp}T_C(t) \\ &\approx AC\mu_C[T_C(t) - \beta_0T_C(t-\eta)] - r_{\rm damp}T_C(t). \end{split} \tag{4}$$

We obtain the usual DO equation:

$$dT_C/dt = R_{\rm DO}T_C(t) - \beta_{\rm DO}T_C(t - \eta), \tag{5}$$

where  $R_{\rm DO} = AC\mu_C - r_{\rm damp}$  and  $\beta_{\rm DO} = A\beta_0 C\mu_C$  are positive constants. From here onward, we skip the notation (t) when the variable is taken at time t without delay.

## 4. Building the RDO model by merging the RO and DO models

#### a. Combining RO and DO equations

The RO captures the long-term recharge of h influencing the SST in the central-eastern Pacific. The DO captures the faster delayed advective-reflective negative feedback influencing the SST in the western-central Pacific. Knowing the importance of central Pacific SST for convection and thus zonal wind, and that the negative feedbacks involved in the DO and RO are physically different, it thus seems relevant to keep these different feedbacks as two distinct processes combined in a hybrid recharge delayed oscillator (RDO), whose set of equations is

$$dT_E/dt = RT_E + F_1 h - \beta T_E(t - \eta), \tag{6}$$

$$dh/dt = -F_2 T_E - \varepsilon h. \tag{7}$$

Equation (6) merges (1) and (5); (7) is the same as Eq. (2). Here central-eastern Pacific  $T_E$  and central Pacific  $T_C$  are merged into one variable representing a single region, the central-eastern Pacific, hereafter  $T_E$  (Niño-3.4 RSST; cf. section 2), for the sake of simplicity. Even though we replace  $T_C$  by  $T_E$ , we still consider  $\eta$  to be about 6 months, because physically

the zonal advection delayed feedback operates more on temperature "weighted" by atmospheric convection sensitivity (cf. below), i.e. more in the central Pacific than in the eastern Pacific (while the recharge thermocline feedback influences more the central-eastern Pacific; cf. the following section).

This RDO simple set of equations sounds conceptually compelling. Notably it does not require the low-frequency approximation (used in Fedorov 2010; Clarke 2010) to be valid, as the RDO takes into account the two main "fast" wave processes, the fast mode adjustment, and the zonal-advective delayed negative feedback.

## b. Confirming the RDO through observations/reanalyses

We now want to verify empirically that this RDO set of equations is justified and statistically grounded, in observations as well as in the 79 CMIP models.

First, we verify that separating the zonal-advective delayed feedback and the recharge process through Eq. (6) makes sense. That is,  $+F_1h$  and  $-\beta T_E(t-\eta)$  represent two distinct physical processes. We do a multivariate linear regression for an equation similar to Eq. (6), but for the tendency of temperature T(x, y, t) anywhere in the tropical Pacific:

$$\partial T(x, y, t)/\partial t = R(x, y)T_E + F_1(x, y)h - \beta(x, y)T_E(t - \eta). \tag{8}$$

The regression quantifies the contributions of  $-\beta(x, y)T_E(t - \eta)$ and  $F_1(x, y)h$  terms to T(x, y, t) tendency at each grid point. Figures 2a and 2b compare their spatial patterns in the tropical Pacific, which are indeed quite different (orthogonal). We see that the  $-\beta T_E(t-\eta)$  contribution is stronger in the westerncentral Pacific, especially near the warm pool eastern edge, where the zonal advection term dominates. It confirms that  $-\beta T_E(t-\eta)$  represents the zonal advective-reflective delayed negative feedback. Conversely, the recharge term  $F_1h$  is larger in the eastern Pacific as expected, as the thermocline feedback term is stronger there (i.e. the recharge/discharge process is more important for EP than for CP El Niño events; e.g. Hasegawa et al. 2006; Kug et al. 2009, 2010; McPhaden 2012; Capotondi 2013; Ren and Jin 2013). Fig. 3a compares more quantitatively their values along the equator. The contribution of  $-\beta T_E(t-\eta)$  is larger than that of  $F_1h$  in the western-central Pacific (around the Niño-4 region), while the contribution of  $F_1h$  is the largest in the central eastern region (from ~150°W, the western boundary of the Niño-3 region), for both obs1 and obs2 datasets (that are consistent, with differences not significant at the 90% level, cf. Fig. S1; while  $\beta$  and  $F_1$  differences are statistically significant). Note that R(x, y, t) is, as  $\beta$ , larger in the ~Niño-4 region (Fig. S1d; likely because of the largest positive Bjerknes feedback there). R is however only about one-third of  $\beta$  there. The correlation skill of Eq. (8a) is high east of the dateline, being at its largest around the Niño-3.4 region (Fig. S1d), where  $\beta$  and  $F_1$  roles add up. This also confirms that focusing on the Niño-3.4 region is a good approximation.

Considering only RSST tendency (Figs. 2a,b), we could think that the recharge term dominates the delayed term.

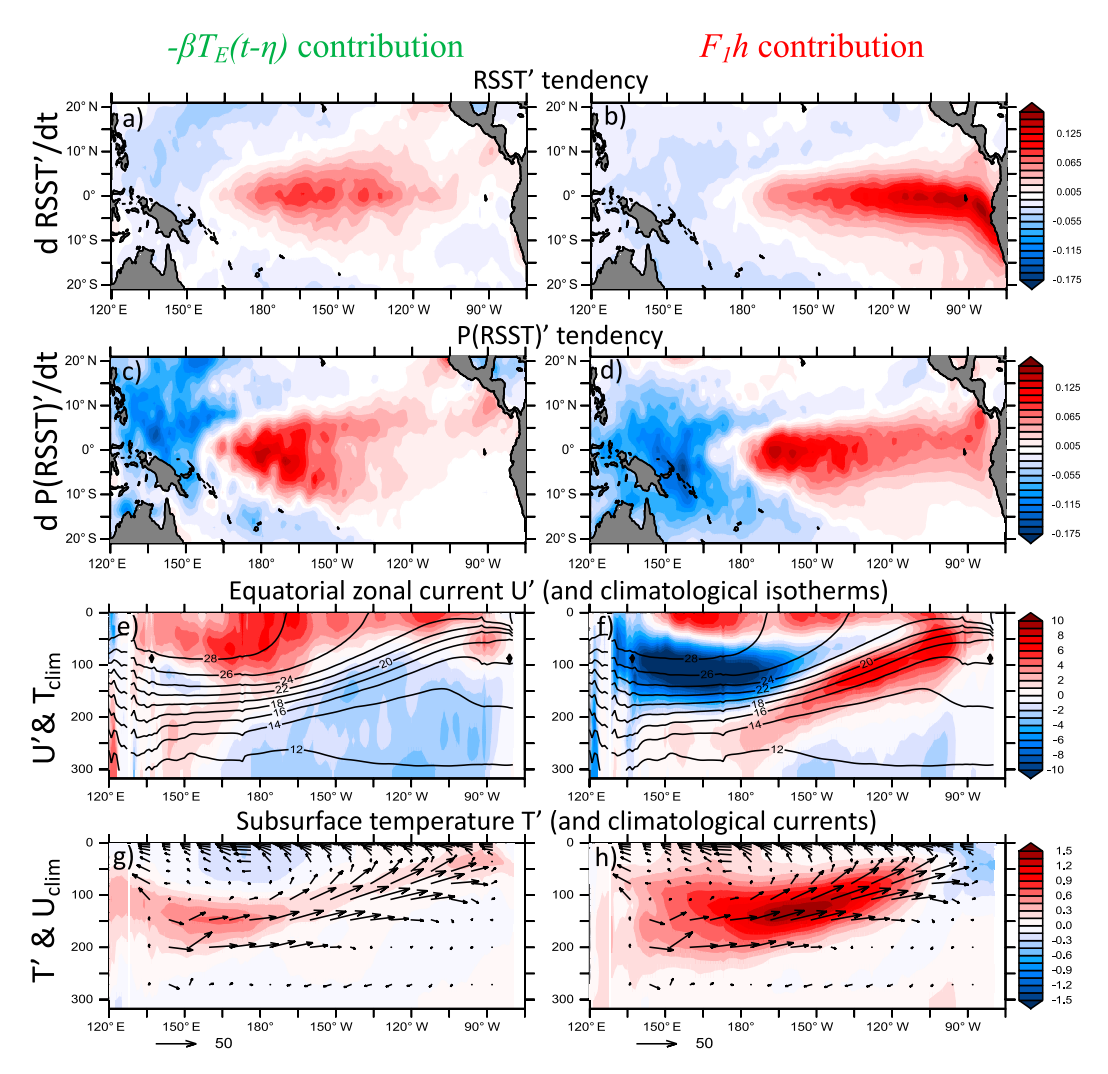


FIG. 2. Distinct physical processes represented by  $-\beta T_E(t-\eta)$  and  $F_1h$  terms in RDO, and related ENSO spatiotemporal diversity captured by the RDO. (a),(b) contributions of, respectively,  $-\beta(x,y)T_E(t-\eta)$  and  $F_1(x,y)h(t)$  to  $\partial T(x,y,t)/\partial t$  in Eq. (8) [i.e. the regression coefficients  $\beta(x,y)$  and  $F_1(x,y)$  for normalized  $T_E$  and h; units:  $^{\circ}$ C month $^{-1}$  per STD of  $T_E$  or h] for obs2. By reconstructing T(x,y,t) from these patterns, the RDO can simulate part of ENSO spatial and spectral diversity (cf. section 4f). (c),(d) As in (a) and (b), but for the expected response of deep convection/precipitation to RSST tendency shown in (a) and (b) (units: mm day $^{-1}$  month $^{-1}$ ), more sensitive to RSST anomalies in the western Pacific warm pool than in the central-eastern cold tongue region [based on Eq. (9):  $P(RSST) = 2e^{0.56RSST}$ ]. (e)–(h) Oceanic mechanisms behind  $-\beta T_E(t-\eta)$  and  $F_1h$  contributions to  $\partial T(x,y,t)/\partial t$ . (e),(f) As in (a) and (b), but for equatorial (2°N–2°S average) subsurface zonal current anomaly U' (color; cm s $^{-1}$ ), with climatological isotherms  $T_{\text{clim}}$  overlayed (black contours; °C). (g),(h) As in (a) and (b), but for subsurface potential temperature anomaly T' (color; °C), with climatological zonal and vertical currents  $U_{\text{clim}}$  and  $W_{\text{clim}}$  overlaid (black vectors; cm s $^{-1}$ ).

Yet, in terms of feedback to deep convection/precipitation/ wind stress, the deep convection (the primary contributor to precipitation in the tropics) sensitivity to RSST anomalies is larger in the western Pacific warm pool region, where climatological RSST is larger, than in the central-eastern cold tongue region [e.g., the He et al. (2018) study had estimated a formula for the precipitation sensitivity to SST, P(SST)]. To illustrate this, we can use a simple exponential formula we have developed as an approximation of the

precipitation sensitivity to local RSST, P(RSST) (appendix Fig. A1):

$$P(RSST) = 2e^{0.56RSST}, (9)$$

where RSST is the total RSST field (including both climatology and anomaly, i.e. RSST<sub>clim</sub> + RSST'). The constant 0.56 is taken from the term representing the effect of RSST on deep convection in Tippett et al. (2011) cyclogenesis index (efficient at

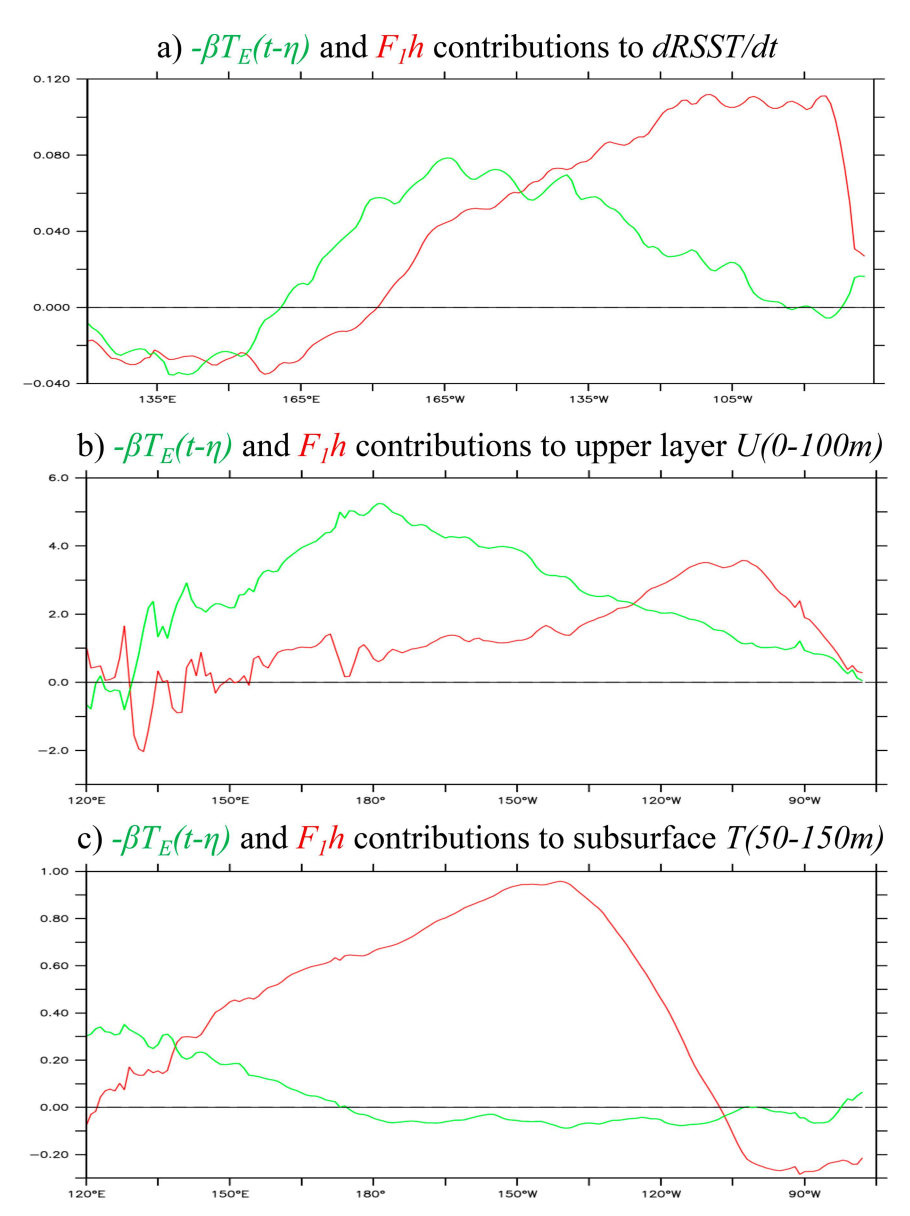


FIG. 3. Equatorial contributions of delayed feedback  $-\beta T_E(t-\eta)$  (green) and of recharge term  $F_1h$  (red). (a) As in Figs. 2a and 2b for RSST tendency, but for the 5°N–5°S average. (b) As in (a), but for upper-layer (0–100 m average) zonal current. (c) As in (a), but for subsurface potential temperature (50–150 m average).

describing the cyclogenesis seasonal cycle at the global scale; Menkes et al. 2012). The factor 2 (in mm day $^{-1}$ ) is a crude fit to the scatterplot of  $\operatorname{Precip}_{\operatorname{clim}}$  to  $\operatorname{RSST}_{\operatorname{clim}}$  in the equatorial Pacific (this factor will anyway not influence the relative contributions to  $dP(\operatorname{RSST})/dt$  of  $-\beta T_E(t-\eta)$  and  $F_1h$  that are our focus here). Figures 2c and 2d are similar to Figs. 2a and 2b, but for  $dP(\operatorname{RSST})/dt$ . The contribution to convective precipitation tendency of  $-\beta T_E(t-\eta)$  has actually, in the western-central Pacific, an almost similar amplitude to the contribution of  $F_1h$ . Note that these estimated contributions to local precipitation will be then amplified by the convergence feedback [conditional instability of

the second kind (CISK)], notably for strong El Niño events in the central-eastern Pacific (Srinivas et al. 2022). To conclude, the  $-\beta T_E(t-\eta)$  term can force large tendencies in precipitation and related equatorial zonal wind stress, crucial for the ocean–atmosphere coupling. Hence, adding the  $-\beta T_E(t-\eta)$  term to the  $\partial T(x, y, t)/\partial t$  equation can make the conceptual model significantly more realistic.

To understand the oceanic mechanisms behind  $-\beta(x, y)$   $T_E(t - \eta)$  and  $F_1(x, y)h(t)$  contributions to  $\partial T(x, y, t)/\partial t$ , remember that the temperature tendency of the oceanic mixed layer is firstly due to heat advection (see its full decomposition in

Fig. S2), with surface fluxes acting to damp interannual SST anomalies. To understand heat advection anomalies, the lower panels of Fig. 2 show equatorial subsurface zonal current anomaly U', with climatological isotherms  $T_{\rm clim}$  overlaid, as well as subsurface potential temperature anomaly T', with climatological currents  $U_{\rm clim}$  and  $W_{\rm clim}$  overlaid.

The  $-\beta T_E(t-\eta)$  contribution is firstly through a large positive U' anomaly in the upper layer. U' is maximal near the dateline [up to 6 cm s<sup>-1</sup> per STD of  $T_E(t-\eta)$ ; Fig. 2e], consistent with the timing of the westward propagation of the equatorial upwelling Rossby wave forced by easterly anomalies 6 months earlier (in the case of a prior La Niña with negative  $T_E$  and easterlies; Fig. 1a was shown for the opposite westerly case). This eastward current anomaly U' advects the negative climatological zonal temperature gradient  $\partial T_{\text{clim}}/\partial x$ , i.e.  $-U'\partial T_{\text{clim}}/\partial x$  (Fig. S3c), favoring a warming of the oceanic mixed layer in the central Pacific [of up to 0.15 K month<sup>-1</sup>, i.e. about 1 K in half a year, per STD of  $T_E(t-\eta)$ ; Fig. S2c]. The T' anomalies related to  $-\beta T_E(t-\eta)$  are conversely weak near the surface [about 0.2 K per STD of  $T_E(t - \eta)$ ; Fig. 2g] and have a secondary role (Fig. S3a) in the heat zonal advection of the mixed layer (and at the subsurface, they are much weaker than those related to  $F_1h$ ; see also Fig. 3c). This analysis confirms that  $-\beta T_E(t-\eta)$  contribution is firstly through zonal advection in the central Pacific, i.e.  $-\beta T_E(t-\eta)$  represents the zonal advective–reflective delayed negative feedback.

The recharge influence  $+F_1h$  represents a different physical process. The  $F_1h$  influence is through warmer EUC and upwelling because of the warm subsurface anomaly in the central-eastern Pacific due to the recharge and related deeper thermocline. The h recharge favors a large subsurface warm anomaly in the heart of the Equatorial Undercurrent (EUC shallower in the east, like the thermocline, from ~150 m at 180° to  $\sim$ 100 m at 130°W). This warm  $T'_{\rm FUC}$  anomaly, partly due to the deeper thermocline (cf. Izumo 2003, 2005), will be advected by the climatological EUC, that is, a positive term  $-U_{\text{clim}}\partial T'/\partial x$  (Fig. S3b). It is also within the climatological equatorial upwelling, that is,  $-W_{\text{clim}}\partial T'/\partial z$  (Fig. S3f). I.e. the EUC will bring warmer waters to the central-eastern Pacific, where they will be upwelled to the mixed layer by the climatological upwelling, favoring an overall warming tendency of the mixed layer of the central-eastern equatorial Pacific (Fig. S2b). Note that there are secondary roles of 1) an increase of the deepest part of the EUC in the east (because of increased zonal gradient of thermocline since the recharge is more in the western-central than in the eastern Pacific), that is,  $-U'\partial T_{\rm clim}/\partial x$  (Fig. S3d), and 2) an upwelling reduction in the extreme east, east of ~100°W, that is,  $-W'\partial T_{\text{clim}}/\partial z$  (Fig. S3h).

To better understand the origin of this warm subsurface anomaly, we have to remember that the EUC is part of a large-scale 3D circulation. It is fed by the north and south meridional pycnocline convergences, at their largest in the western Pacific. They are the lower branches of the shallow subtropical/tropical cells (STCs/TCs; McCreary and Yu 1992; McCreary and Lu 1994; Zeller et al. 2019, 2021). The south convergence is climatologically 2 times larger than the north

one (because of the potential vorticity barrier in the north) and is the first origin of EUC waters (Blanke and Raynaud 1997; Stellema et al. 2022). Hence, the h recharge associated to deeper thermocline in the equatorial and southwest Pacific favors warmer transport-weighted temperatures of the meridional pycnocline convergences, notably the dominant south convergence related to southwest Pacific recharge, thereby feeding the EUC with warmer waters (Izumo 2003, 2005; Ballester et al. 2015, 2016). Note by the way that the north-south asymmetry in the convergence further justifies the use of the asymmetric recharge index  $h_{\rm eq+sw}$ .

Figures 3b and 3c summarize the distinct dominant oceanic processes for the delayed feedback (green line) and recharge term (red). The delayed feedback dominates for U' in the west and central Pacific upper layer (i.e. for zonal advection  $-U'\partial T_{\rm clim}/\partial x$ ). The recharge term dominates for the subsurface temperature anomaly T' advected by the mean 3D circulation (i.e. by the climatological EUC through  $-U_{\rm clim}\partial T'/\partial x$ ) and by climatological upwelling through  $-W_{\rm clim}\partial T'/\partial z$  in most of the equatorial Pacific.

Overall, these analyses confirm from observations/reanalysis that this RDO is physically grounded, the two terms  $-\beta T_E(t-\eta)$  and  $F_1h$  being both important and representing distinct physical processes. It is hence more physical to distinguish these two terms, Eq. (6) being one reasonable way to conceptualize them. Furthermore, we will show later that the different spatial patterns of  $\beta$  and  $F_1$  seen in Figs. 2a and 2b allow the RDO to capture partly the ENSO spatiotemporal diversity in equatorial Pacific T(x, y, t). But for now, we will firstly analyze the RDO in its simplest form, focusing on spatially averaged Niño-3.4 RSST, namely,  $T_E(t)$ .

A second way of confirming the relevance of the RDO [Eq. (6)] is to compute the coefficients R,  $F_1$ , and  $\beta$  obtained from the multivariate linear regression of  $dT_E/dt$  onto  $T_E(t)$ , h(t), and  $T_E(t-\eta)$  for observations (and in the following section for CMIP models), now focusing on the tendency of spatially averaged  $T_E$ , as shown in the very left of Fig. 4a for observations. The most striking result is that  $F_1$  and  $\beta$  are both highly significantly positive in obs1 and obs2 (at the 95% level). Therefore, both need to be taken into account, and cannot be neglected in Eq. (6). Consistently, observed h and  $T_E(t-\eta)$  have more than half ( $\sim$ 60%) of unshared variance, in agreement with the fact that they firstly represent different physical processes.

# c. Confirming the RDO through the CMIP multimodel database; mean state influence

Accordingly, the RDO equation is also relevant for most CMIP models, with  $F_1$  and  $\beta$  being both significantly positive in almost all the CMIP models (Fig. 4). In the following, we write variable  $X = X1[X2]\{X3\}$  with X1 for values obtained with "obs1" (OISST and satellite SLA), X2 for "obs2" (HadISST and ORAS5 SLA) and X3 for the multimodel mean (MMM) of CMIP5 and CMIP6 historical runs. CMIP MMM values lie within observational uncertainties:  $(F_1, \beta) = (0.14 \pm 0.03, 0.06 \pm 0.04) [0.11 \pm 0.02, 0.09 \pm 0.02]$  month<sup>-1</sup> for observations and  $\{0.11 \pm 0.02, 0.07 \pm 0.02\}$  for CMIP (similar values for

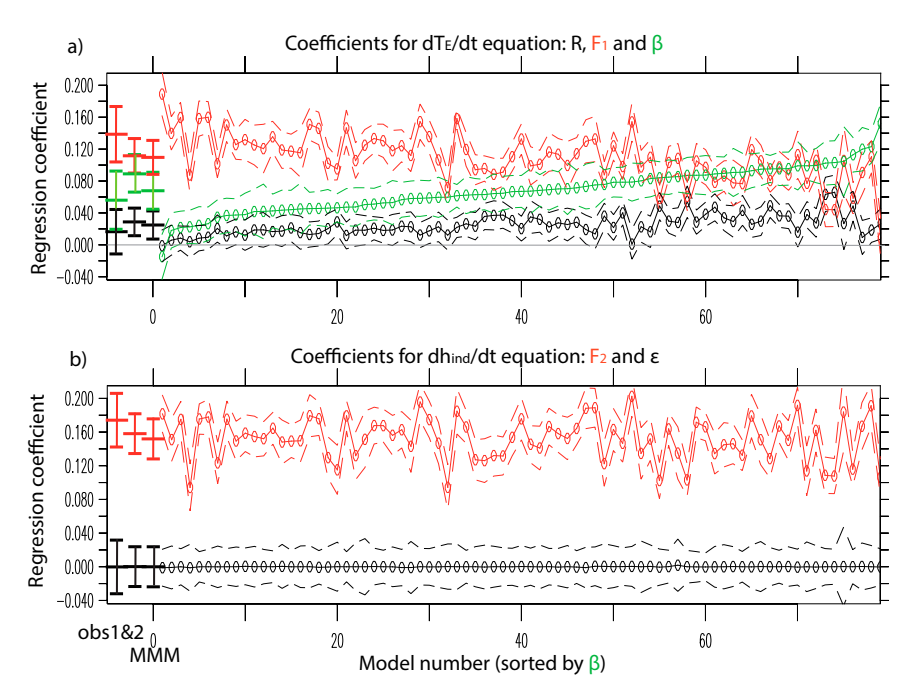


FIG. 4. Significance of the RDO coefficients in observations and CMIP. (a) Coefficients R (black),  $F_1$  (red), and  $\beta$  (green) of the regression of  $dT_E/dt$  onto normalized  $T_E(t)$ , h(t), and  $T_E(t-\eta)$  [cf. Eq. (6)] for the 79 CMIP models sorted by  $\beta$  (numbers 1 to 79 on x axis). (b) Coefficients  $F_2$  (red) and  $\varepsilon$  (black) of the regression of dh/dt onto  $T_E(t)$  and h(t) [cf. Eq. (2)]. Three thick error bars from the left to right respectively show obs1, obs2, and the multimodel mean (MMM).  $T_E$  and h are normalized so that regression coefficients (units: month<sup>-1</sup>) can be compared, whatever the model's ENSO amplitude. The 90% confidence intervals are shown as dashes, and for observations and MMM as markers.

CMIP5 and CMIP6 MMM). Note that the relative strengths of  $F_1$  and  $\beta$  can also depend on the period used (consistent with the fact that the dominant ENSO flavor may have changed with time). For example, longer obs2 can be compared to obs1 on their 26-yr-long overlapping period, 1993-2018. It gives  $(F_1, \beta) = [0.13 \pm 0.02, 0.06 \pm 0.02] \text{ month}^{-1}$ , almost similar to obs1, with  $F_1$  larger than  $\beta$ . While obs2 on the 26-yr earlier period 1959–84 gives  $(F_1, \beta) = [0.09 \pm 0.02, 0.10 \pm 0.02]$ month<sup>-1</sup>, with conversely  $F_1$  weaker than  $\beta$  [possibly because of higher-frequency ENSO during that period; cf. section 4; such decadal changes could partly explain the changes in observed  $WWV/T_E$  lag relationship shown by McPhaden (2012) and confirmed by Crespo et al. (2022)]. The R coefficient is weaker,  $R = 0.02 \pm 0.03 [0.03 \pm 0.02] \{0.02 \pm 0.02\} \text{ month}^{-1}$ , but is still significantly positive at the 90% level in the majority of CMIP models in this new RDO framework, contrary to  $R_{\rm RO}$  that is not significantly different from zero in the pure RO framework. The correlation skill of the RDO  $dT_E/dt$ equation, (6), is highly significant ( $r_{T_r} = 0.71[0.68]\{0.64\}$  also confirming the RDO relevance. The Steiger's test (on the difference between these two dependent correlations from a single sample; note that the correlations are overlapping, sharing one variable in common) allows us to compute the significance of the improvement of the skill (and of its square, i.e. explained variance) in obs1 (obs2): from RO to RDO, this significance is 84% (97%) [explained variance

increases from 48% to 51% (41% to 46%)], and from DO to RDO, it is 99% (99%) [explained variance increases from 34% to 51% (35% to 46%)]. For CMIP MMM, the improvement is even more significant statistically, given the much longer time series: the explained variance increases by ~10% from RO to RDO (from 34% to 38%) and by ~20% from DO to RDO (from 29% to 38%). Note that, in the most realistic version of the RDO, the nonlinear seasonal RDO developed later, the improvement is even much larger (section 5).

Interestingly, there is a large CMIP intermodel diversity in the relative strengths of the coefficients  $F_1$  and  $\beta$ , larger than for R (Fig. 4a). The models (sorted by the amplitude of  $\beta$  in Fig. 4) that have a large  $F_1$  tend to have a weak  $\beta$ , and vice versa (intermodel correlation = -0.69). Note that R is positively correlated with  $\beta$  (0.59) and negatively correlated with  $F_1$  (-0.75). This large diversity of the parameters is likely related to the diversity of spectral, spatial and amplitude (related to growth rate) characteristics of ENSO and of Pacific mean state (cf. below) among CMIP models.

Figure 4b similarly shows the coefficients  $F_2$  and  $\varepsilon$  for the regression of dh/dt onto  $T_E(t)$  and h(t).  $F_2$  is highly significant in all observations and models,  $F_2 = 0.17 \pm 0.03[0.16 \pm 0.02]$  {0.15  $\pm$  0.02} month<sup>-1</sup> and more consistent in amplitude among CMIP than  $F_1$  and  $\beta$ , with a weaker intermodel diversity ( $\sim \pm 30\%$  of MMM value) positively correlated with  $F_1$ 

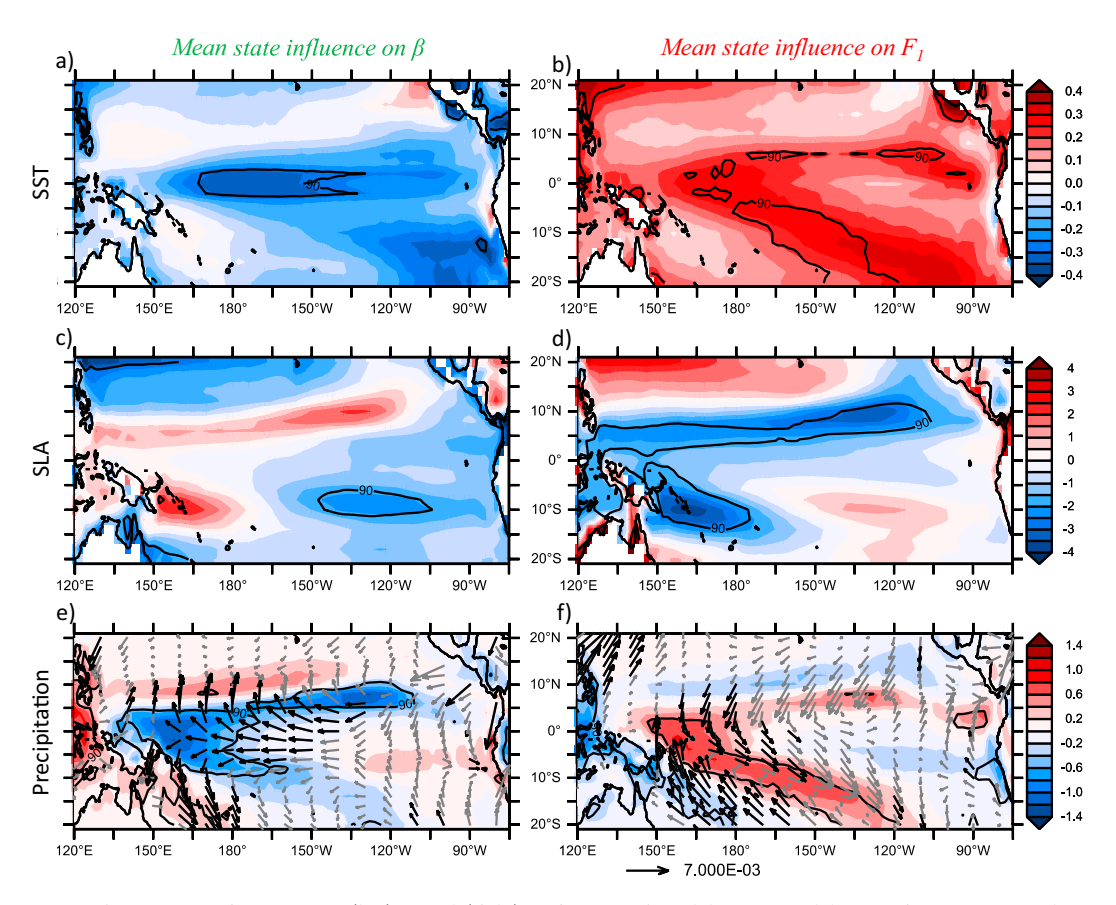


FIG. 5. Mean-state influence on (left)  $\beta$  and (right)  $F_1$  in CMIP5 models. Intermodel regressions, onto  $\beta$  and  $F_1$  separately, of model mean state, in terms of (top) SST (units: K), (middle) SLA (with SLA global mean removed; units: cm), and (bottom) precipitation (units: mm day<sup>-1</sup>; wind stress overlaid in gray, and in black when significant at the 90% level, vectors direction adjusted to panels aspect ratio; units: N m<sup>-2</sup>; 90% significant level overlaid as black contours; two-tailed Student's t test). Amplitudes per intermodel STD of  $\beta$  or  $F_1$ .

(intermodel correlation = 0.79). As in observations,  $\varepsilon$  is negligible in all CMIP models [confirming Izumo and Colin's (2022) result for CMIP models: using an independent index such as "h" =  $h_{\text{ind\_eq+sw}}$  rather than other recharge indices polluted by the tilt mode component leads to a negligible  $\varepsilon$ ; note that we expect oceanic dissipation to be weak, e.g. Fedorov 2010]. The correlation skill of the regression is again highly significant:  $r_h = 0.67[0.67][0.57]$ .

CMIP MMM is qualitatively similar to observations, but each model has its own biases. One may hence question how sensitive these results are to ENSO realism in CMIP models. So we have evaluated ENSO in each CMIP model by its ENSO amplitude [STD( $T_E$ )] and spectral shape [namely the ratio between the spectral density in the 1–3-yr band and that in the 3–15-yr band, i.e. STD (1/3–1/1 yr<sup>-1</sup> band-pass filtered Niño-3.4 RSST) divided by STD (1/15–1/3 yr<sup>-1</sup> band-pass filtered Niño3.4 RSST), close to Bellenger et al. (2014) metrics; more detailed evaluations of CMIP ENSO can be found in earlier references; e.g. Bellenger et al. 2014]. We have found some models that are quite far from observations for these two metrics, especially in CMIP5. We then selected the most realistic CMIP models and have redone Fig. 4 for them

(Fig. S4). Consistently, the models with the lowest  $\beta$  values (on the left) are rejected, as well as most models with the largest  $\beta$  values. But anyway, the MMM of the RDO parameters are almost similar (to the MMM of all models without selection) for this set of selected models (as well as for CMIP5 and CMIP6 separately). These verifications confirm that the results here are robust,  $\beta$  becoming even more statistically significant when selecting the most realistic models.

The next step is to understand what causes the intermodel diversity in RDO parameters. Knowing that  $\beta$  and  $F_1$  represent distinct physical processes, we expect their strengths to have distinct dependances to the mean state of the climate model. They should depend notably on the SST zonal gradient, the position of the warm pool eastern edge, the mean thermocline depth, themselves possibly related to the typical cold tongue bias, or to the western Pacific precipitation bias (e.g. Bayr et al. 2018, 2019) with double ITCZ (intertropical convergence zone) bias and related SPCZ (South Pacific convergence zone) bias. We can explore this in e.g. CMIP5 models. Figure 5 shows the intermodel regressions of model mean state (in terms of SST, SLA, precipitation, and wind stress) onto  $\beta$  and  $F_1$  separately. Note that the patterns related to  $\beta$ 

and  $F_1$  might seem opposite to each other at first glance, but they are actually quite different, not simply opposite in sign.  $\beta$ is as expected larger if the cold tongue is stronger in a model (Fig. 5a), i.e. if the negative mean zonal SST gradient in the western-central equatorial Pacific is stronger (Bayr et al. 2018). The stronger cold tongue there is itself related to larger equatorial easterlies related to larger precipitation over the Maritime Continent and weaker precipitation in the central Pacific with a horseshoe pattern (Fig. 5e).  $F_1$  strength is more correlated to SLA/thermocline depth mean state (Fig. 5d). A possible explanation is the following: the shallower the mean thermocline is in the southwestern and equatorial Pacific [and also at the southern edge of the north ITCZ, where the North Equatorial Counter Current (NECC) is located], the shallower the STCs lower branches are, the more their transportweighted temperatures can be affected by thermocline depth anomalies related to a recharged or discharged state. The SLA/thermocline depth mean state changes in Fig. 5d are interestingly related not only to equatorial zonal wind stress and equatorial cold tongue, but also to meridionally asymmetric off-equatorial wind stress and related curl (with notably Ekman pumping in the SPCZ forcing off-equatorial Rossby waves propagating westward in the southwest Pacific) associated with mean precipitation (and SST) asymmetric changes (Fig. 5f). To sum up, the strength of the delayed feedback and

the effectiveness of the recharge/discharge process vary as a result of the CMIP mean state diversity.

For simplicity, we choose the default values  $F_1 = 0.12$ ,  $\beta = 0.08$ , R = 0.02,  $F_2 = 0.16$ , and  $\varepsilon = 0$  month<sup>-1</sup>, as a simple example to represent their typical values. With these default parameters, the delayed term contribution is two thirds of the recharge term contribution in the temperature tendency equation.

## d. RDO eigenvalues and their dependency to parameters

The solutions of the RDO system of differential equations are a vector space, actually of infinite dimension because of the delayed term (see details later on and see also Jin 1997a). To understand the RDO behavior and dependency to parameters, we obtain the eigenvalues by considering complex solutions of the form  $e^{\sigma t}$ , with  $\sigma = \sigma_r + i\sigma_i$ , its real part  $\sigma_r$  being the exponential growth or damping rate, and its imaginary part  $\sigma_i$  being the angular frequency. The set of Eqs. (6) and (7) (with  $\varepsilon$  here neglected for the sake of simplicity; including it is straightforward but makes the below equations heavier; not shown) leads to the following eigenvalues characteristic equation:

$$\sigma^2 - R\sigma + \beta\sigma e^{-\sigma\eta} + F_1 F_2 = 0. \tag{10}$$

This equation in the complex space is equivalent to two real equations:

$$\begin{split} &\sigma_r^2 - \sigma_i^2 - R\sigma_r + \beta e^{-(\sigma_r\eta)}[\sigma_r\cos(\sigma_i\eta) + \sigma_i\sin(\sigma_i\eta)] + F_1F_2 = 0 \quad \text{[real part of (10)]}, \\ &2\sigma_r\sigma_i - R\sigma_i + \beta e^{-(\sigma_r\eta)}[\sigma_i\cos(\sigma_i\eta) - \sigma_r\sin(\sigma_i\eta)] = 0 \quad \quad \text{[imaginary part of (10)]}. \end{split}$$

The solutions can be found numerically as the intersections of the solutions of each of these last two equations in the  $(\sigma_r, \sigma_i)$ space (Fig. S5). The pure DO has an infinity of solutions, while the pure RO has only one. Therefore, the RDO eigenvalues in Eq. (10) have an infinity of solutions and the model has an infinity of eigenmodes. Around the default values of the parameters, the first mode is a weakly-damped low-frequency mode (close to observed ENSO main period, and with characteristics relatively close to the RO single mode), with a ~3-yr period and a  $\sim 0.02 \text{ month}^{-1}$  damping rate (i.e.  $\sim 1/4 \text{ yr}^{-1}$ ). The second mode is a highly-damped higher-frequency mode (~5-month period and  $\sim 0.45 \text{ month}^{-1}$  damping rate). This second mode can add some high-frequency behavior, making the RDO more appealing than the pure RO which only has one eigenmode close to the first RDO mode. Higher eigenmodes are even more damped and of higher frequency.

The eigenvalues in Eq. (10) depend on parameters R,  $\beta$  and on the product  $F_1F_2$ , i.e. on the Wyrtki angular frequency  $W = (F_1F_2)^{1/2}$ , on which the eigenfrequency depends in the RO framework (cf. Lu et al. 2018; Jin et al. 2020). Figures S6d–f show the dependency of RDO eigenfrequency  $f = \sigma_f/(2\pi)$  to W,  $\beta$ , and R separately. Ranges of W, B, and B are chosen by considering the observations uncertainties and the intermodel diversity in CMIP data shown in Fig. 4a. For these ranges, the dependency of RDO eigenfrequency to W and B is larger than for the range of B seen in observations and CMIP. Thus, we

just focus on the dependency to W and  $\beta$  (Fig. 6b). Both W and  $\beta$  will increase the eigenfrequency similarly. The isofrequency lines can be crudely approximated as diagonal lines with a negative slope close to -1. Actually, if the isofrequency lines were exactly diagonal lines with a negative slope equal to -1 (cf. slope of the overlaid diagonal line) and monotonically increasing with W and  $\beta$  in that Fig. 6b, that would mean that f would be proportional to the sum  $W + \beta$ ; i.e.,  $f \sim f_0 + S(W + \beta)$ , where  $f_0$  and S would be approximately constant within the CMIP parameter range (with approximately  $f_0 \sim 0.008 \text{ month}^{-1}$  and  $S \sim 0.09$ ). The intermodel diversity in RDO eigenfrequency (or also qualitatively in ENSO spectral shape) should hence be approximately proportional to the sum  $W + \beta$ . Indeed, the ENSO spectral shape in CMIP models is roughly linearly related to  $W + \beta$ , as evidenced by Fig. 6c, with a high intermodel correlation of 0.75 between  $W + \beta$  and ENSO spectral shape among models. The correlation drops to only 0.43 or 0.30 when only W or  $\beta$  alone is used instead of their sum  $W + \beta$  (note: correlation with W alone here less good than in Lu et al. (2018) because here W is evaluated from the multi-regression fit for the RDO; in their study the pure RO is considered, so that their recharge term  $F_{1 \text{ RO}}$  will then mix statistically  $F_{1}$  and  $\beta$  contributions). The sum  $W + \beta$  thus explains well the diversity of ENSO frequency among CMIP models. It represents the combined effects of the recharge and delayed feedback processes on ENSO frequency diversity in CMIP models.

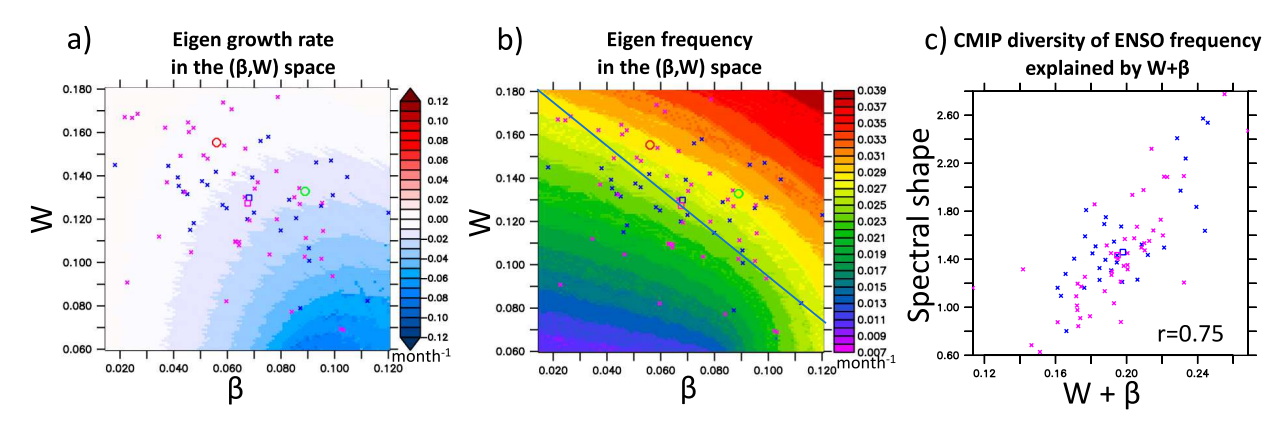


FIG. 6. Dependency of RDO eigenvalues to parameters. (a) RDO eigen growth rate (color shading; units: month<sup>-1</sup>) as a function of both  $\beta$  and Wyrtki angular frequency  $W = (F_1F_2)^{1/2}$  (W being the eigen angular frequency of the pure RO). (b) As in (a), but for eigenfrequency (blue diagonal line showing  $W = -\beta + \text{constant}$ ). (c) ENSO spectral shape metric (higher values when ENSO frequency increases, cf. section 2) as a function of the sum  $W + \beta$  for each CMIP5 (blue) and CMIP6 (purple) model (with their MMM in squares). In (a) and (b), circles show obs1 (red) and obs2 (green).

The eigen growth rate  $\sigma_r$  has a complex dependence to W and  $\beta$  (Fig. 6a;  $\sigma_r$  dependence to W,  $\beta$  and R separately shown in Figs. S6a-c). Around CMIP MMM, an increase in W increases  $\sigma_r$ , i.e. decreases the damping, while an increase in  $\beta$ increases the damping. Around W and  $\beta$  default values,  $\sigma_r$  increases quasi-linearly with R (Fig. S6c), i.e. with the Bjerknes feedback:  $\sigma_r \approx 0.6 \ (R - 0.04)$  (for the RO, we would have  $\sigma_r = (R_{\rm RO} - \varepsilon)/2 \approx 0.5 R_{\rm RO}$ ; Jin et al. 2020). The diversity of these parameters may relate to the diversity in ENSO frequency and ENSO amplitude among models. Interestingly, obs1 as well as about half of CMIP models are near criticality (i.e. almost undamped). If the combination of the three parameters leads to a sufficiently large  $\sigma_r$  so as to become positive, it would lead to an instability. Could this explain some ENSO nonlinearities? Or some tipping point effects? Further work would be needed to test this.

#### e. RDO response to stochastic forcing

Now we analyze the RDO response to stochastic forcing. Stochastic forcing is required, as the RDO is damped for the default parameters. To better understand the conceptual model behavior, we have forced the RDO by adding two realistic red noises, one,  $\mu_T$ , in the right-hand side (rhs) of  $T_E$  [Eq. (6)] and one,  $\mu_h$ , in the rhs of h [Eq. (7)]. The STDs of these red noises  $(\sigma_T \approx \sigma_h \approx 0.18 \text{ month}^{-1})$  are inferred from the two observed residuals of the linear regression fits of Eqs. (6) and (7). These noises are chosen to be independent, as the two observed residuals are only weakly correlated [shared variance < 10%; see also Takahashi et al. (2019) sensitivity tests on this kind of noise choice]. Figure 7a first shows an example of the  $T_E$  synthetical time series obtained for default parameter values. The system has oscillations, with a frequency modulation, and with low- and high-variance decades (similar results over the full 1000-yr period; not shown). The RDO spectral response consistently has a broad peak between ~4 and ~2-yr periods, maximal at ~3-yr (black curve in Fig. 7c), roughly consistent with observed ENSO. Figure 7b shows the typical evolution of

the different terms of the  $dT_E/dt$  equation during an ENSO event (i.e. lag regression onto  $T_E$ ) for the default synthetic time series shown in Fig. 7a. h (red curve) leads  $T_E$  (light blue) by  $\sim 10$  months, i.e. about a quarter of the ENSO period, as expected because a recharge in h favors a positive  $T_E$  [Eq. (6)], as for usual RO. The delayed feedback effect has a different timing. It is the first to favor the phase reversal, followed by the recharge process. In the RDO, the *negative* noise forcing at lag  $\sim -20$  months can already force indirectly the following El Niño onset, notably through the delayed feedback 6 months later. And a *positive* noise (from about -10 months before ENSO peak) can of course also force an El Niño directly.

While most contributions are qualitatively similar in obs1 and obs2 (shown in Fig. S7 for comparison) and are within observations confidence intervals, there are also interesting differences. Observed asymmetries are, by construction, not captured by the simplest RDO framework with only linear terms (cf. sections 5 and 6), e.g.: 1) nonlinearities and external forcing included in the residual in Eqs. (6) and (7) are possibly large during ENSO development and mature phase, and damp the reversal to ENSO opposite phase (with the observed second peak of the residual at  $\sim$ 10-month lag not seen for the synthetic time series); 2) the advective-reflective delayed negative feedback seems to play a larger and more systematic role for ENSO events termination and for La Niña onset than for El Niño onset (Fig. S7 composites). In summary, within its linear limits, the linear nonseasonal RDO framework qualitatively matches observations and could help us to better understand the interplay between the recharge and advective-reflective delayed feedbacks in shaping the real-world ENSO.

To illustrate how sensitive the RDO spectral response is to the strength of the advective–reflective delayed negative feedback  $\beta$ , Fig. 7c shows the RDO spectral response for a smaller (0.05) or larger (0.13)  $\beta$  (its default value being 0.08 month<sup>-1</sup>). In the small  $\beta$  case, the response is of lower frequency (period  $\sim$  3.3 years) and less damped, with a sharper peak (closer to RO harmonic oscillator behavior). In the large  $\beta$  case, the

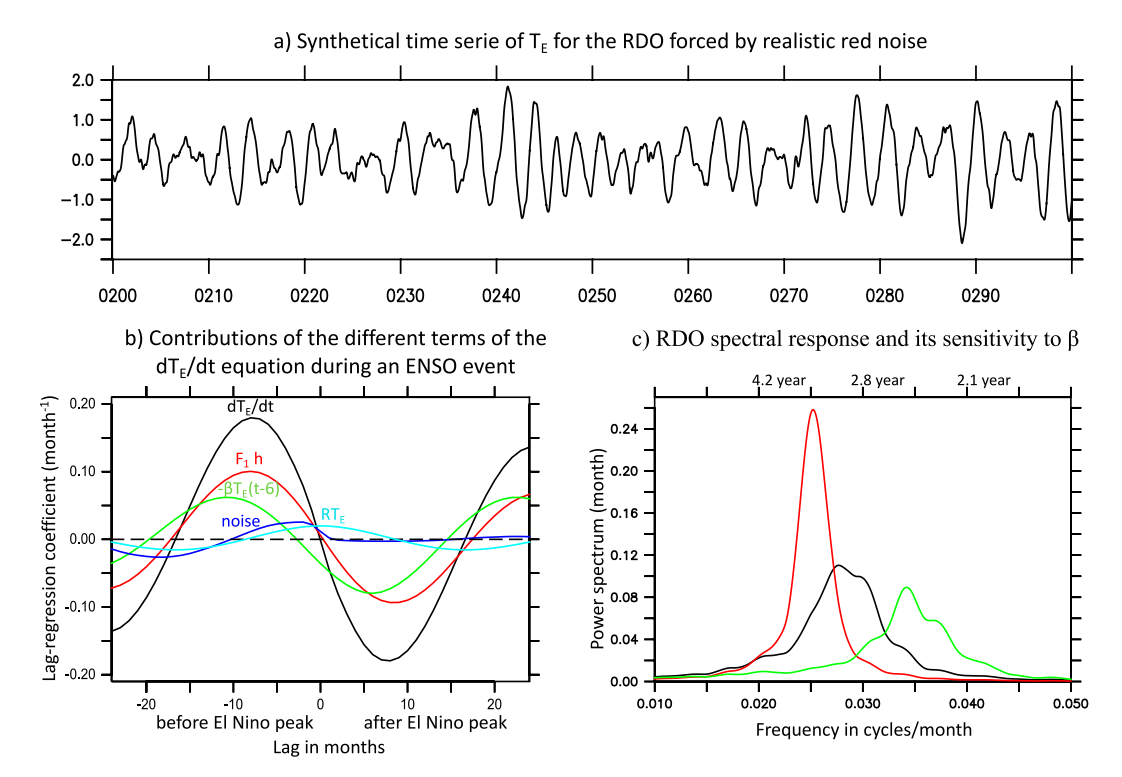


FIG. 7. RDO response to stochastic forcing. (a) Synthetical time series of  $T_E$  for the linear RDO forced by realistic red noises [added to the rhs of Eqs. (6) and (7); STD( $T_E$ ) = 0.7 for 1000 years]. (b) The different terms of the  $dT_E/dt$  equation, (6), lag-regressed onto  $T_E$ , showing their various contributions (units: month<sup>-1</sup> per STD of  $T_E$ ) during the evolution of an ENSO event:  $dT_E/dt$  (black),  $F_1h$  (red),  $-\beta T_E(t-\eta)$  (green),  $RT_E$  (cyan; which also indicates ENSO phase), and red noise forcing  $\sigma_T$  (dark blue). The x axis shows the lag, with negative lags before ENSO peak and positive lags after ENSO peak. (c) RDO spectral response (i.e., frequency response to white noise: power spectrum of  $T_E$  for a 1000-yr long white noise forcing) for  $\beta$  default value (0.08 month<sup>-1</sup>; black), a larger  $\beta$  (0.13 month<sup>-1</sup>; green; i.e.; closer to pure DO with a quasibiennial QB mode) and a smaller  $\beta$  (0.05 month<sup>-1</sup>; red; i.e., close to pure RO with a quasiquadrennial QQ mode; for the small  $\beta$  case, the much larger power spectrum is divided by 3 for visualization).

response is of higher frequency (period  $\sim 2.5$  years) and highly damped, with a broader spectral range (closer to DO behavior). This broader spectral response can be explained because the DO has a much broader spectral response, thanks to its infinite number of eigenmodes, than the RO, which has only one eigenfrequency. That is, the delayed negative feedback brings spectral diversity to the RDO spectrum. To sum up, ENSO spectrum and amplitude are very sensitive to  $\beta$ , i.e. to the advective–reflective delayed negative feedback strength (itself related to the climatological SST zonal gradient).

# f. ENSO spatio-temporal diversity in the RDO framework

The RDO model, even in its simplest form, can also explain part of ENSO spatial diversity. To illustrate this, we can exploit the multivariate linear regression based on Eq. (8) for the tendency of temperature T(x, y, t) anywhere in the tropical Pacific. As seen earlier (Figs. 2a,b), the  $\beta(x, y)$  contribution reminds us of the central Pacific (CP) El Niño spatial pattern, and the  $F_1(x, y)$  contribution reminds us of the eastern Pacific (EP) El Niño pattern.

Hence, when the RDO is forced by noise, we will have different spatial patterns of T(x, y, t), closer to CP or EP spatial pattern depending on the relative contributions of  $\beta$ and  $F_1$  terms (that notably depend on the frequency of stochastic forcing). The spatial and temporal properties of ENSO are thus strongly dependent on which of the recharge  $F_1$  or delayed  $\beta$  effect is locally dominant. Indeed, we can reconstruct "offline" T(x, y, t) at any location by integrating temporally Eq. (8) [i.e. the linear combination of  $T_E(t)$ , h(t) and  $T_E(t-\eta)$ ], after having obtained synthetic time series of  $T_E$  and h from the RDO forced by noise (e.g. time series shown in Fig. 7a). As an example, we have reconstructed T(x, y, t) from the 1000-yr-long synthetic time series of  $T_E$  and h, using the averages of obs1 and obs2 for the regression coefficients R(x, y),  $F_1(x, y)$ , and  $\beta(x, y)$ [reconstructed T(x, y, t) is high-pass filtered, like long obs2, to remove multidecadal variability that can arise from the time integration, so as to focus on interannual timescales]. We can then compare for instance reconstructed Niño-4 (CP) and Niño3 (EP) SST variabilities. Niño-4 is of significantly higher frequency than Niño-3, with an almost-doubled spectral shape metrics: 2.7 for Niño-4, 1.5 for

Niño-3. This is because Niño-3 is dominated by  $F_1h$ , and h is essentially the integral of  $T_E$ , and thus of lower frequency than  $T_E$ . While Niño-4 is dominated by  $-\beta T_E(t-\eta)$ , which has the same spectrum as  $T_E$ . The RDO can thus, even in its simplest form, simulate some ENSO spatiotemporal diversity. The RDO captures the fact that part of the CP variability is more biennial (QB) because the delayed feedback is dominant there, and that the EP variability is more quadrennial (QQ; e.g. Wang and Ren 2017) because the slower recharge feedback is dominant there. Note that additionally, there is in observations a decadal component of CP ENSO (Behera and Yamagata 2010; Sullivan et al. 2016; Capotondi et al. 2020) that could be implemented in the RDO framework, e.g. through a decadal modulation of the mean state (e.g. Zhang et al. 2019) modulating RDO parameters (possibly through STCs; Zeller et al. 2019, 2021).

#### 5. Nonlinear seasonal RDO

The simplest RDO framework, linear and nonseasonal, can be obviously improved by adding: 1) the seasonal cycles of RDO parameters and 2) asymmetries/nonlinearities (e.g. quadratic terms and a multiplicative noise). We have added them separately, and then all together in the most comprehensive RDO version, the nonlinear seasonal RDO. We have also tested the influence of each nonlinear parameter on the phase diagram trajectories (supplemental material). The take-home message is that, with seasonal cycle, nonlinearities and multiplicative noise added, the RDO is even more realistic, and still has robust and highly significant  $F_1$  and  $\beta$  coefficients (i.e. the nonlinear seasonal RDO is more realistic than the nonlinear seasonal RO or DO).

#### a. Seasonality of RDO parameters

Knowing the ENSO observed seasonal phase-locking, the first improvement to do to the RDO is to allow all its parameters to vary seasonally. The simplest seasonality we can add for parameters is, for instance for  $\beta$  parameter, of the form  $\beta = \beta_0 + \beta_{\text{seas}} \sin(\omega t - \lambda) = \beta_0 + \beta_S \sin(\omega t) + \beta_C \cos(\omega t).$ The  $\beta = \beta_0 + \beta_{\text{seas}} \sin(\omega t - \lambda)$  format looks mathematically "nicer" by having amplitude  $\beta_{seas}$  and phase  $\lambda$  separately rather than  $\beta = \beta_0 + \beta_S \sin(\omega t) + \beta_C \cos(\omega t)$ . Yet the latter form is more convenient, notably to compute intervals of confidence and when we want to compare different observations and/or models, as the phase  $\lambda$  is modulo( $2\pi$ ) and we for instance cannot compute a multimodel mean (MMM) of  $\lambda$  directly from the  $\lambda$  of each model (it would only be possible by first computing the  $\beta_S$  and  $\beta_C$  MMM, to then convert them into  $\beta_{\text{seas}}$  and  $\lambda$  values). And  $\beta_S$  and  $\beta_C$  are straightforward to interpret: here t = 0 on 1 January, so that  $sin(\omega t)$  is maximum on 1 April and minimum on 1 October, and  $cos(\omega t)$  is maximum on 1 January and minimum on 1 July. As the number of parameters to fit is now multiplied by 3 (i.e., equal to 9 for the  $T_E$  tendency equation and equal to 6 for the h one), we essentially focus on the results based on our longest reanalysis data, 'hist', and on CMIP historical runs, for which the number of effective degrees of freedom is sufficiently large (obs2

still shown in Fig. S8; note however the larger uncertainty bars when estimating RDO seasonally varying parameters with obs2; obs1 is not shown, being obviously too short). In a nutshell, the correlation skills  $r_T$  and  $r_h$  of  $dT_E/dt$  and dh/dt equations strongly increase by including the seasonal cycle [cf. Figs. S8b,c]. And the RDO still has a robust and highly significant  $\beta$  coefficient for the delayed feedback (with  $\beta_0$  even 2 times larger than  $F_{1,0}$  in hist; Fig. S8c).

Let us now describe each parameter's seasonal cycle (Figs. 8a-c shown here for the nonlinear version of the seasonal RDO, which has a similar seasonality to its linear version; cf. comparison of each parameter's seasonal coefficients in Fig. S8). We here focus on hist-based parameters, as this should be our most realistic estimates, keeping in mind the limits of historical oceanic reanalyses, the actual "truth" being possibly between hist, shorter obs2, and CMIP estimates. To interpret the coefficients seasonality, keep in mind that their actual contribution to  $T_E$  and htendencies will be the product of the coefficient and of its associated term. For example, the  $F_2T_E$  actual contribution to dh/dt will be larger in boreal winter than  $F_2$  alone, when  $T_E$  interannual STD peaks. Let us start with R. R has a strong seasonal cycle, with  $-R_S \sim R_0 > 0$ . R is the largest around September and the lowest in March, favoring a peak of ENSO around December, as expected from previous studies (e.g. Jin et al. 2020).  $F_1$  has a relatively weak seasonal cycle, being slightly larger around January-March and weaker around July-September, likely because the climatological equatorial upwelling in the central-eastern Pacific (170°-120°W) is the strongest in January-March and the weakest in July-September.  $\beta_0$  is highly significant (even above 99% level). It is larger than  $F_{1,0}$  in hist (but not in obs2 and CMIP).  $\beta$  has a large seasonal cycle, dominated by  $\beta_S$ , i.e. is maximal in spring, possibly because of the seasonal cycle in the product  $C\mu_C$ between the coupling parameter  $\mu_C$  and the climatological zonal SST gradient C (cf. section 3b), and/or because of Indian Ocean dipole (IOD, an equivalent of El Niño for the Indian Ocean, e.g., Saji et al. 1999) delayed influence (Izumo et al. 2010) likely partly included in the delayed term. The difference between  $F_1$  and  $\beta$  seasonal cycles further confirms that  $F_1$  and  $\beta$  terms represent distinct physical processes.

For dh/dt [Eq. (7)], which is the same for the RO and RDO, previous studies (e.g. Chen and Jin 2020) of the RO had usually considered  $F_2$  to be seasonally constant, supposing that its seasonal cycle was negligible. Actually,  $F_2$  has a large significant and robust seasonality in all our estimates (Figs. 8a–c and Fig. S8). This is the first study to our knowledge that shows this  $F_2$  seasonality for the RO/RDO recharge equation.  $F_2$  represents the efficiency of the recharge for a given  $T_E$  anomaly (e.g. of 1 STD).  $F_{2,S}$  is as large as the constant component  $F_{2,0}$  in hist.  $F_2$  is maximum in early spring (February–April) and negligible in early autumn (August–October), with of course differences among observations and CMIP estimates.  $\varepsilon_0$  is weakly positive,  $\sim$ 0.02 month<sup>-1</sup>, with some seasonal cycle, maximum in hist ( $\varepsilon_S < 0$ ) in fall and negligible in spring. Taking into account all these

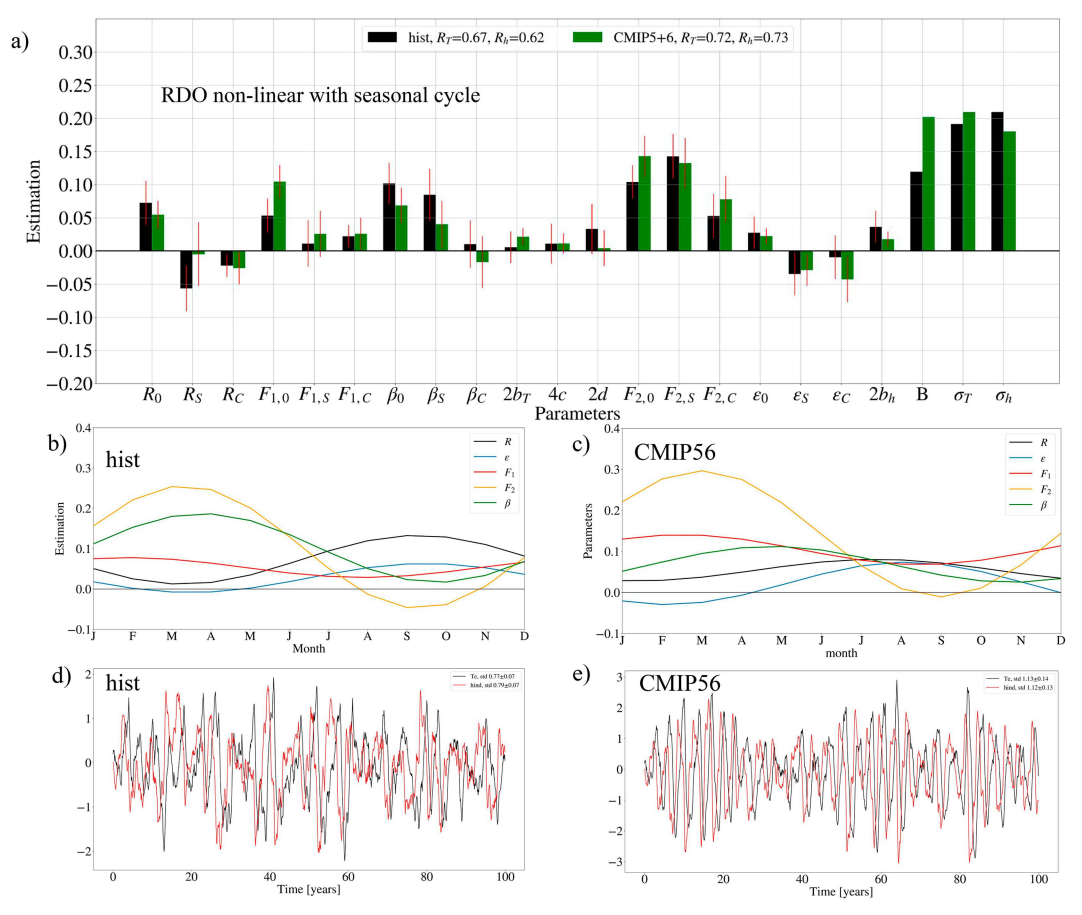


FIG. 8. The nonlinear seasonal RDO. (a) Bar plot showing each parameter of Eqs. (11) and (12), estimated by a multivariate fit (with B and  $\sigma_T$  estimated as in An et al. 2020b). To represent the actual contribution of the nonlinear terms for strong ENSO events, their parameters are multiplied by 2 for quadratic terms and by 4 for the cubic term for a fair comparison with linear parameters such as R,  $F_1$ , and  $\beta$  (as for a strong 2STD event, we will have, e.g.,  $F_1T_E = 2F_1$ ,  $b_TT_E^2 = 2 \times 2b_T$ ,  $cT_E^3 = 2 \times 4c$ ). The correlation skills  $r_T$  and  $r_h$  are given above the bar plots. For hist (black), the red line shows the 95% interval of confidence. For CMIP MMM (green), it represents the  $\pm 1$  intermodel STD (among all CMIP). (b) Seasonal cycles of the main RDO parameters estimated from the fit on hist. (c) As in (b), but for CMIP MMM. (d) A 100-yr-long time series of hist-based nonlinear seasonal RDO (STD given for the average of fifty 100-yr-long timeseries). (e) As in (d), but for CMIP-based RDO.

seasonal cycles lead to a more realistic RDO behavior with seasonal phase-locking and richer combination tones (e.g. Stuecker et al. 2013), especially when including nonlinearities, i.e. the full nonlinear seasonal RDO version described hereafter.

#### b. Adding nonlinearity: The nonlinear seasonal RDO

Above we had neglected asymmetries/nonlinearities for the sake of simplicity. The next step is to include such terms. We can add to the  $dT_E/dt$  [Eq. (6)] the quadratic and cubic terms  $+b_TT_E^2-cT_E^3+dT_Eh$ . They notably represent the nonlinear response of convection (and of related wind stress) to  $T_E$  (e.g. Choi et al. 2013; Takahashi et al. 2019; Jin et al. 2020; An et al. 2020a; Dommenget and Al Ansari 2023; Srinivas et al. 2022; G. Srinivas et al. 2024, unpublished manuscript). We can also add a multiplicative noise [e.g. Jin et al. 2007; Graham et al. 2015, their Eq. (23)]. We can add to the dh/dt

[Eq. (7)] a quadratic term  $-b_H T_E^2$ . That is, the discharge during an El Niño of amplitude  $T_{E,0}$  is larger than the recharge during a La Niña of similar amplitude  $-T_{E,0}$ , notably because equatorial zonal wind stress anomalies are of larger amplitude and fetch (G. Srinivas et al. 2024, unpublished manuscript) and are farther to the east [e.g. Izumo et al. 2019; note that we could add even further complexity, e.g. a nonlinearity of the delayed term, as in DiNezio and Deser (2014), and a state dependency of  $F_2$  as in Iwakiri and Watanabe (2022) to even better simulate long-lasting La Niña]. Thus, the nonlinear seasonal RDO equations are

$$dT_E/dt = RT_E + F_1h - \beta T_E(t - \eta) + b_T T_E^2 - cT_E^3 + dT_E h + \mu_T (1 + BT_E),$$
(11)

$$dh/dt = -F_2 T_E - \varepsilon h - b_h T_E^2 + \mu_h, \tag{12}$$

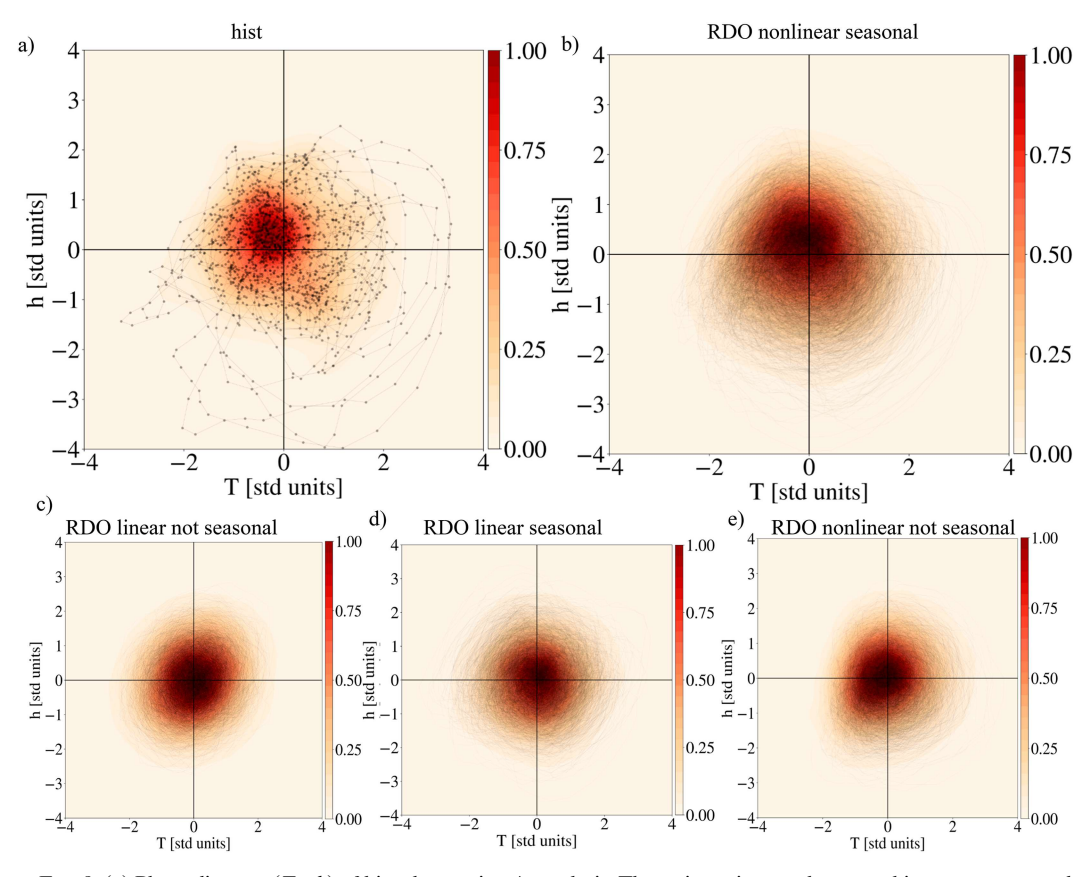


FIG. 9. (a) Phase diagram ( $T_E$ , h) of hist observations/reanalysis. The trajectories are shown as thin gray curves, and their probability density function (PDF, scaled by its maximum) as color shading. (b) Phase diagram ( $T_{E\_synthetic}$ ,  $h\__{synthetic}$ ) of fifty 100-yr-long synthetical time series obtained by forcing hist-based nonlinear seasonal RDO by red noises. (c) As in (b), but for the hist-based simplest linear RDO without seasonality (and without multiplicative noise, i.e., B=0). (d) As in (c), but adding seasonality. (e) As in (c), but adding nonlinearities (including multiplicative noise). Note that when the distribution is shifted with extreme El Niño and discharge being stronger, the PDF maximum, i.e., the most likely points, is shifted toward slightly negative  $T_E$  and positive h anomalies (mean removed).

where  $\mu_T$  and  $\mu_h$  are red noises with standard deviations  $\sigma_T$  and  $\sigma_h$  respectively, and with a 5-day decorrelation time (cf. section 2); B represents the strength of the multiplicative noise (i.e. larger noise during El Niño than during La Niña). Here we have tried to keep the notations as much as possible consistent with the (soon-to-be open-source) Community RO model under development presently, in which we participate [S.-K. Kim et al. 2024, unpublished manuscript; related to the review of Vialard et al. (2024, unpublished manuscript); see also the notations in the review of An et al. (2020a)].

Now we have 12 parameters to fit for Eq. (11) (as we assume no seasonality of the nonlinear terms, and as B and  $\sigma_T$  are separately estimated from the residual distribution), and 7 parameters for Eq. (12), shown in Fig. 8a and Fig. S8. The first result is that the RDO is still robust and better than the RO, when including nonlinearity and multiplicative noise in addition to seasonality. The term  $\beta_0$  is large and significant (even at the 99% level in hist and CMIP). Including this delayed effect to the RO clearly increases the skill and explained variance of  $dT_E/dt$  equation (in hist: correlation skill  $r_T=0.60$  to 0.67, i.e. a relative increase of explained variance by 25%,

 $r_T^2$  increasing from 36% to 45%; in CMIP:  $r_T = 0.67$  to 0.72, i.e. increase of explained variance by 16%,  $r_T^2$  increasing from 45% to 52%). The results for CMIP and hist are qualitatively consistent, but quantitatively different. The largest differences are for  $F_1$  and  $\beta$  relative contributions,  $\beta$  being larger than  $F_1$ in hist (vice versa for CMIP), as aforementioned. The nonlinearities d and  $b_h$  are stronger in hist. Figures 8d and 8e show the generated synthetic time series of  $T_E$ , for hist and CMIP-MMM parameters respectively. They are quite different too. The synthetic time series for hist look more realistic (asymmetry, irregularity). Most CMIP models have a bias in ENSO nonlinearity/asymmetry (Hayashi et al. 2020); thus, that their RDO also fails to reproduce asymmetry is expected. The larger irregularity of hist-based RDO could be partly explained by the larger  $\beta/F_1$  ratio in hist than in CMIP. Figure 9b shows the trajectories in the  $(T_E, h)$  phase space of the histbased nonlinear seasonal RDO. They are qualitatively similar to hist ones (Fig. 9a), with similar asymmetries, namely larger extreme El Niño events with larger and faster discharges than extreme La Niña [see, e.g., Iwakiri and Watanabe (2022) for processes driving long-lasting La Niña].

To highlight visually the role of each nonlinear term in the nonlinear seasonal RDO (for the set of parameters obtained from hist), Fig. S9 shows RDO phase diagram when each of them is artificially removed. E.g. the absence of  $b_h T_E^2$  in Fig. S9b leads to less extreme discharge (there is still some asymmetry in the recharge/discharge due to the nonlinear terms in the  $dT_E/dt$  equation, but weaker than with  $b_h$  included). That is, Fig. S9b shows that the  $b_h T_E^2$  role makes the discharge more extreme during strong El Niño. Multiplicative noise associated to B sustains strong El Niño (i.e. the lower-right quarter of the phase diagram; Fig. S9d). The role of  $b_T T_E^2$  should be to increase El Niño and reduce La Niña. However, in the hist case shown here where  $b_T$  is weak, this effect is hard to see in Fig. S9e (it would be more seen in CMIP-based RDO case). The cubic term  $-cT_E^3$  reduces very extreme  $T_E$  events (for both El Niño and La Niña events; Fig. S9f). The  $dT_E h$  favors larger "La Niña+discharged state" events in the lower-left quadrant and diminishes them in the upperright quadrant, "tilting" the phase diagram. Note that this detailed analysis of the role of each nonlinear term remains qualitatively valid for the RO framework.

#### 6. Conclusions

#### a. Summary

We have developed a hybrid recharge delayed oscillator, the RDO, more realistic than the stand-alone RO or DO (schematics in Fig. 1). This RDO can help us to improve our theoretical understanding of ENSO and of its irregularity, diversity, and complexity. We have shown that the ENSO temperature tendency  $dT_E/dt$  results essentially from the combination of two distinct negative feedback mechanisms with distinct spatial distributions, in addition to the Bjerknes positive feedback:

- 1) the slow long-term recharge during La Niña (discharge during El Niño) with a time scale of ~1–2 years. This slow recharge process takes place over the equatorial and southwestern Pacific independently of the fast tilt mode, i.e., "h" = h<sub>ind\_eq+sw</sub>. This long-term recharge firstly affects the oceanic mixed layer temperature tendency in the central-eastern equatorial Pacific by favoring advection of warmer subsurface waters by the climatological STCs/TCs and EUC towards the equatorial upwelling, i.e., −U<sub>clim</sub>∂T'/∂x and −W<sub>clim</sub>∂T'/∂z.
- 2) the advective-reflective delayed negative feedback of ~6 months. This delayed feedback firstly affects the oceanic mixed layer temperature tendency in the western-central equatorial Pacific by anomalous upper layer zonal current advecting the climatological temperature zonal gradient through wave processes, i.e., -U'∂T<sub>clim</sub>/∂x.

These two *distinct* processes are both essential for equatorial Pacific SST variability and so for the coupled system. Hence, rather than stating that the recharge oscillator (RO) and delayed oscillator (DO) are two different formal ways of representing the same physical process as done usually in previous studies, the present results based on observations and 79 CMIP models show that these two different physical processes with different

timescales should be distinguished in the equations. They can be formally incorporated in the RDO. This hybrid oscillator has qualitatively realistic spectral characteristics (with a wider spectral peak than the RO) and lead-lag relationships. The inclusion of the delayed term  $-\beta T_E(t-\eta)$  [with  $\eta=6$  months] favors a more irregular, and possibly chaotic, behavior when forced by stochastic forcing. RDO eigenvalues are highly sensitive to both the Wyrtki angular frequency  $W = (F_1F_2)^{1/2}$  and the  $\beta$  parameter (representing respectively the strengths of the RO and DO components), themselves sensitive to the mean state (and thus to CMIP model biases). We have notably shown that the main RDO eigenfrequency is approximately linearly related to the sum  $W + \beta$ . That is, ENSO frequency increases not only if W is larger, but also if the advective-reflective delayed feedback is larger. Furthermore, by taking into account that the advectivereflective delayed feedback (respectively recharge feedback) is larger in the western-central Pacific (respectively eastern equatorial Pacific), each feedback having its own time scale, we can reconstruct equatorial SST at any longitude within the RDO framework, and simulate some ENSO spatiotemporal diversity.

Finally, we have shown that the simple RDO framework is robust and more realistic than the RO framework, and could be significantly improved by adding: 1) the seasonal cycles of RDO parameters, 2) asymmetries/nonlinearities, e.g. quadratic/cubic terms and a multiplicative noise. These nonlinearities added to seasonality further increase the system's complexity and possibly make it more irregular and chaotic, and thus increase potentially ENSO spatiotemporal diversity. We have also investigated the influence of each nonlinear term on the  $(T_E, h)$  phase space trajectories, an investigation that is also useful for the RO framework.

## b. Discussion on possible improvements of the RDO

This latest and more refined nonlinear seasonal RDO version could still be further improved by adding 1) influences external to the tropical Pacific and 2) a third box in the model to explicitly allow for more spatial diversity of ENSO events.

External influences to add are notably the two-way interaction of the IOD with ENSO (e.g. Izumo et al. 2010, 2014; Luo et al. 2010; Jourdain et al. 2016), the mean tropical Indian and Atlantic Oceans warming/cooling, which act as negative feedbacks to ENSO (e.g. Dommenget and Yu 2017), and the north and south tropical Pacific (e.g. Alexander et al. 2010). For example, the IOD can also force the advective–reflective delayed feedback: a negative IOD forces easterly anomalies in the western Pacific, thereby favoring positive zonal current anomalies ~6 months later in the western-central equatorial Pacific. Hence a perspective would be to add a third variable in the system, the IOD as a forcing external to the tropical Pacific coupled to ENSO [mathematically like in Kug and Kang (2006) and Frauen and Dommenget (2012), but for the IOD rather than for the Indian Ocean basinwide SST].

Here our original aim was not to capture the various ENSO flavors, i.e. the ENSO diversity continuum from extreme EP El Niño to CP El Niño Modoki events, that have partly distinct global teleconnections. For the sake of simplicity, we have focused on ENSO events defined with the usual Niño-3.4 region. Still, the RDO framework has allowed us to reconstruct ENSO

spatiotemporal diversity, at least partly, even without adding nonlinear terms (Figs. 2a,b). While in the RO framework, nonlinearities are needed to capture ENSO diversity (Thual and Dewitte 2023). Adding seasonality and nonlinearities to the RDO (section 5) can increase simulated ENSO diversity/complexity even more. The next step is to implement our RDO approach in a three-box conceptual model (i.e. west, central, and east Pacific boxes), such as in Fang and Mu (2018), Geng et al. (2020), and Chen et al. (2022) but with a physically based formalization of the equations inspired by the above RDO approach.

#### c. Implications and perspectives

The RO still remains useful, being the simplest ENSO conceptual model. We still appreciate its use. But it implicitly mixes two physically different processes, the zonal advective and thermocline feedbacks. The RDO does not. It is more physical and captures the spatial and frequential diversity of ENSO, while still remaining simple enough.

The RDO set of equations may formally look partly like a simplification of the unified oscillator of Wang (2001), which was shown by Graham et al. (2015) to be less realistic than the simple DO. However, here the RDO set of equations is for  $(T_E, h_{\text{ind\_eq+sw}})$  orthogonal space instead of  $(T_E, h_{\text{eq}})$  nonorthogonal space. And the various terms of the RDO equations represent clear distinct physical mechanisms, conversely to the unified oscillator as pointed out by Graham et al. (2015).

For ENSO operational forecast diagnostics, Izumo and Colin (2022) have shown that the pair of coordinates  $(T_E, h_{\text{ind\_eq+sw}})$  is more relevant to describe the RO system trajectory than the usual pairs  $(T_E, h_{\text{eq}})$  or  $(T_E, h_w)$ . Here the RDO realism furthermore suggests that an additional useful term to take into account to operationally diagnose the system state is  $T_E(t-\eta)$  as an indicator of the advective–reflective delayed negative feedback effect, e.g. when diagnosing the present oceanic state or for operational forecasts. The RDO framework should also be useful to study ENSO predictability with information theory (Fang and Chen 2023).

Background interdecadal changes in the sum  $W + \beta$  may favor the quasi-quadrennial (QQ) or quasi-biennial (QB) ENSO regimes (e.g. Jin et al. 2020) and might have a role in ENSO "regime shifts" and ENSO diversity. The QQ regime is more associated with large EP El Niño events, for which the thermocline feedback (W) plays a central role. While the QB regime is more associated with moderate CP El Niño events more driven by the zonal advection feedback ( $\beta$ ). The RDO framework (possibly adding a third box as suggested above) could help us in understanding the differences between the decades with weak and strong ENSO variances and with differences in ENSO frequency and flavors, possibly related to decadal mean state changes influencing  $\beta$  and W relative strengths (Chen et al. 2022; Chen and Fang 2023), as well as the ENSO response to climate change (e.g. Cai et al. 2021; Shin et al. 2022).

There are several pathways to better understand theoretically the RDO model. How combining the RO and DO influences the chaotic behavior of the delayed differential equation system (e.g. Tziperman et al. 1995; Keane et al. 2016), as for the case of

two coupled oscillators interacting with noise. A mathematical approach with series as in Power (2011) for the DO could be developed for the RDO. For the nonlinear seasonal RDO, an approach based on a Fokker–Planck equation could help (An et al. 2020b). Then we could use an intermediate approach similar to Yu et al. (2016), who combined the RO to a slab ocean coupled to an AGCM to capture ENSO dynamics and diversity. But we could modify their intermediate model by 1) using an independent recharge index such as  $h_{\rm ind\_eq+sw}$ , 2) adding the delayed negative feedback with its shorter timescale.

The RDO could help us to reconcile ENSO theories. It would be very interesting to redo detailed analyses testing each ENSO oscillator, such as Graham et al. (2015) approach, and/or Linz et al. (2014) approach based on transfer functions, in light of the present results, and see whether theories, climate models, and observations would better agree if one keeps RO and DO processes distinguished through the hybrid RDO framework developed here. To conclude, using this simple RDO framework could help us to improve ENSO theories, climate model diagnostics, and forecasts.

Acknowledgments. First, we would like to thank the three reviewers for their highly relevant reviews. They have pushed us to demonstrate even further the RDO framework potential, and have also clearly improved the readability of the manuscript. T. I. would like to thank his excellent former student, Timothée Jullien de Pommerol, for downloading the CMIP6 data, and for implementing a first Python version of the nonlinear seasonal RO, that B. P. has then further improved, as well as Jérôme Vialard and Matthieu Lengaigne for interesting discussions at a much earlier stage of this work. M. C. would like to thank Steven Sherwood for his essential support, supervision, and mentoring, in particular throughout the pandemic, which made this collaboration possible. We also would like to thank Soong-Ki Kim, Sen Zhao, and Jérôme Vialard for interactions and discussions on the nonlinear seasonal RO implemented by B. P. in Python in the Community RO Model framework initiated by Jérôme Vialard (who we really thank for this excellent initiative). T. I. and M. C. would like to thank the UPF team for their continuing support, as well as for hosting M. C. because of COVID-related closed Australian borders; this latter fact was paradoxically essential for allowing us to make this work mature. T. I. and B. P. are funded mainly by IRD core budget, with some funding from UMR241 SECO-POL (ex-EIO) laboratory and ANR ARISE project.

Data availability statement. All data used are open data: OISSTv2 (https://psl.noaa.gov/data/gridded/data.noaa.oisst.v2. html), ERA5 and ORAS5 (https://www.ecmwf.int), Copernicus SLA (https://doi.org/10.48670/moi-00148), SODA (https://www2.atmos.umd.edu/~ocean/), Tropflux (https://incois.gov.in/tropflux/), HadISSTv1.1 (https://www.metoffice.gov.uk/hadobs/hadisst/), CMIP models (https://wcrp-cmip.org), GPCP (https://psl.noaa.gov/data/gridded/data.gpcp.html), and 20CR (https://psl.noaa.gov/data/20thC\_Rean/). We acknowledge the use of NOAA pyferret open-source software for analyses and figures, as well as python.

#### **APPENDIX**

## A Simple Exponential Formula for the Precipitation Sensitivity to Relative Sea Surface Temperature

Figure A1 illustrates the validation of the approximated exponential formula for the precipitation sensitivity to local RSST that we have developed in section 4b:

$$P(RSST) \approx 2e^{0.56RSST}$$
 [Eq. (9)].

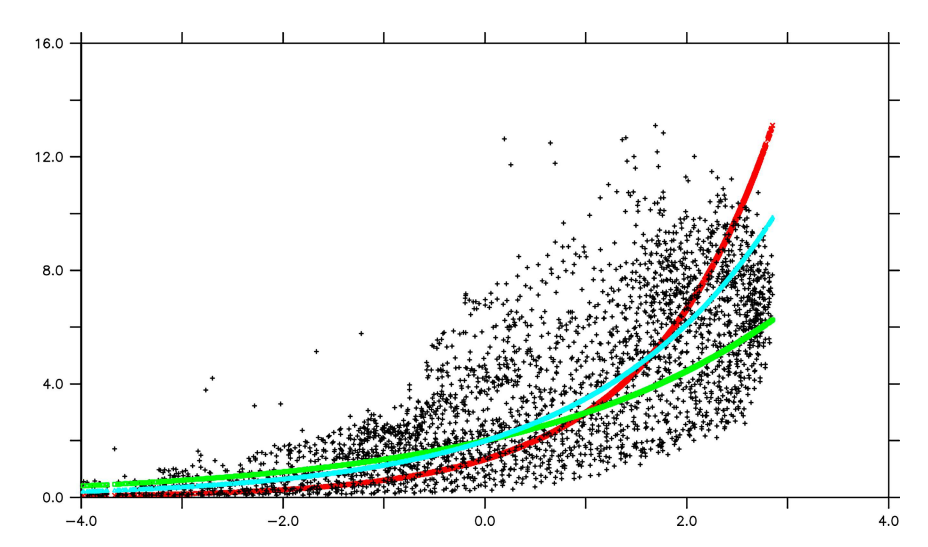


FIG. A1. Verification of the approximated formula for the sensitivity of precipitation to RSST. Scatterplot of Precip<sub>clim</sub> (monthly GPCP precipitation; units: mm day  $^{-1}$ ) to RSST<sub>clim</sub> (monthly OISST, regridded on GPCP grid; units: K) in the equatorial Pacific (5°N–5°S, 120°E–80°W). The default fit in blue is  $P(RSST) = 2e^{0.56RSST}$ , the factor 0.56 inspired by the Tippett et al. cyclogenesis index. Tests using other exponential forms, e.g.,  $P(RSST) = 2e^{0.4RSST}$  (green) or  $P(RSST) = 2e^{0.8(RSST-0.5)}$  (red) show that the default approximation is qualitatively reasonable. Figures 2c and 2d redone with these other forms lead to qualitatively similar results, with delayed term contribution increasing if the factor in the exponential increases, as it gives more weight to regions with higher climatological RSST (vice versa if it decreases).

#### REFERENCES

Adler, R. F., and Coauthors, 2003: The version-2 Global Precipitation Climatology Project (GPCP) monthly precipitation analysis (1979–present). *J. Hydrometeor.*, **4**, 1147–1167, https://doi.org/10.1175/1525-7541(2003)004<1147:TVGPCP>2.0.CO;2.

Alexander, M. A., D. J. Vimont, P. Chang, and J. D. Scott, 2010: The impact of extratropical atmospheric variability on ENSO: Testing the seasonal footprinting mechanism using coupled model experiments. J. Climate, 23, 2885–2901, https://doi.org/ 10.1175/2010JCLJ3205.1.

An, S.-I., E. Tziperman, Y. M. Okumura, and T. Li, 2020a: ENSO irregularity and asymmetry. El Niño Southern Oscillation in a Changing Climate, Geophys. Monogr., Vol. 253, Amer. Geophys. Union, 153–172, https://doi.org/10.1002/9781119548164.ch7.

—, S.-K. Kim, and A. Timmermann, 2020b: Fokker–Planck dynamics of the El Niño–Southern Oscillation. Sci. Rep., 10, 16282, https://doi.org/10.1038/s41598-020-73449-7.

Ashok, K., S. K. Behera, S. A. Rao, H. Weng, and T. Yamagata, 2007: El Niño Modoki and its possible teleconnection. *J. Geophys. Res.*, **112**, C11007, https://doi.org/10.1029/2006JC003798.

Ballester, J., S. Bordoni, D. Petrova, and X. Rodó, 2015: On the dynamical mechanisms explaining the western Pacific subsurface temperature buildup leading to ENSO events. *Geophys. Res. Lett.*, 42, 2961–2967, https://doi.org/10.1002/2015GL063701.

—, —, and —, 2016: Heat advection processes leading to El Niño events as depicted by an ensemble of ocean assimilation products. *J. Geophys. Res. Oceans*, **121**, 3710–3729, https://doi.org/10.1002/2016JC011718.

Battisti, D. S., and A. C. Hirst, 1989: Interannual variability in a tropical atmosphere–ocean model: Influence of the basic state, ocean geometry, and nonlinearity. *J. Atmos. Sci.*, **46**, 1687–1712, https://doi.org/10.1175/1520-0469(1989)046<1687: IVIATA>2.0.CO;2.

Bayr, T., M. Latif, D. Dommenget, C. Wengel, J. Harlaß, and W. Park, 2018: Mean-state dependence of ENSO atmospheric feedbacks in climate models. *Climate Dyn.*, 50, 3171–3194, https://doi.org/10.1007/s00382-017-3799-2.

—, C. Wengel, M. Latif, D. Dommenget, J. Lübbecke, and W. Park, 2019: Error compensation of ENSO atmospheric feedbacks in climate models and its influence on simulated ENSO dynamics. *Climate Dyn.*, **53**, 155–172, https://doi.org/ 10.1007/s00382-018-4575-7.

- Behera, S., and T. Yamagata, 2010: Imprint of the El Niño Modoki on decadal sea level changes. *Geophys. Res. Lett.*, **37**, L23702, https://doi.org/10.1029/2010GL045936.
- Bellenger, H., É. Guilyardi, J. Leloup, M. Lengaigne, and J. Vialard, 2014: ENSO representation in climate models: From CMIP3 to CMIP5. Climate Dyn., 42, 1999–2018, https://doi.org/10.1007/s00382-013-1783-z.
- Blanke, B., and S. Raynaud, 1997: Kinematics of the Pacific equatorial undercurrent: An Eulerian and Lagrangian approach from GCM results. J. Phys. Oceanogr., 27, 1038– 1053, https://doi.org/10.1175/1520-0485(1997)027<1038: KOTPEU>2.0.CO;2.
- Boulanger, J.-P., and C. Menkes, 2001: The Trident Pacific model. Part 2: Role of long equatorial wave reflection on sea surface temperature anomalies during the 1993–1998 TOPEX/ POSEIDON period. Climate Dyn., 17, 175–186, https://doi. org/10.1007/PL00013734.
- —, and M. Lengaigne, 2004: Role of high- and low-frequency winds and wave reflection in the onset, growth and termination of the 1997–1998 El Niño. *Climate Dyn.*, **22**, 267–280, https://doi.org/10.1007/s00382-003-0383-8.
- Bunge, L., and A. J. Clarke, 2009: A verified estimation of the El Niño index Niño-3.4 since 1877. J. Climate, 22, 3979–3992, https://doi.org/10.1175/2009JCLI2724.1.
- Cai, W., and Coauthors, 2021: Changing El Niño–Southern Oscillation in a warming climate. *Nat. Rev. Earth Environ.*, 2, 628–644, https://doi.org/10.1038/s43017-021-00199-z.
- Capotondi, A., 2013: ENSO diversity in the NCAR CCSM4 climate model. J. Geophys. Res. Oceans, 118, 4755–4770, https://doi.org/10.1002/jgrc.20335.
- —, and Coauthors, 2015: Understanding ENSO diversity. Bull. Amer. Meteor. Soc., 96, 921–938, https://doi.org/10.1175/ BAMS-D-13-00117.1.
- —, A. T. Wittenberg, J. S. Kug, K. Takahashi, and M. J. McPhaden, 2020: ENSO diversity. El Niño Southern Oscillation in a Changing Climate, Geophys. Monogr., Amer. Geophys. Union, 65–86, https://doi.org/10.1002/9781119548164.ch4.
- Chen, H.-C., and F.-F. Jin, 2020: Fundamental behavior of ENSO phase locking. *J. Climate*, 33, 1953–1968, https://doi.org/10. 1175/JCLI-D-19-0264.1.
- Chen, N., and X. Fang, 2023: A simple multiscale intermediate coupled stochastic model for El Niño diversity and complexity. J. Adv. Model. Earth Syst., 15, e2022MS003469, https:// doi.org/10.1029/2022MS003469.
- —, and J.-Y. Yu, 2022: A multiscale model for El Niño complexity. *npj Climate Atmos. Sci.*, **5**, 16, https://www.nature.com/articles/s41612-022-00241-x.
- Choi, K.-Y., G. A. Vecchi, and A. T. Wittenberg, 2013: ENSO transition, duration, and amplitude asymmetries: Role of the nonlinear wind stress coupling in a conceptual model. *J. Climate*, 26, 9462–9476, https://doi.org/10.1175/JCLI-D-13-00045.1.
- Clarke, A. J., 1994: Why are surface equatorial ENSO winds anomalously westerly under anomalous large-scale convection? *J. Climate*, **7**, 1623–1627, https://doi.org/10.1175/1520-0442(1994)007<1623:WASEEW>2.0.CO;2.
- —, 2008: An Introduction to the Dynamics of El Niño and the Southern Oscillation. Academic Press, 324 pp.
- —, 2010: Analytical theory for the quasi-steady and low-frequency equatorial ocean response to wind forcing: The "tilt" and "warm water volume" modes. *J. Phys. Oceanogr.*, 40, 121–137, https://doi.org/10.1175/2009JPO4263.1.

- —, S. Van Gorder, and G. Colantuono, 2007: Wind stress curl and ENSO discharge/recharge in the equatorial Pacific. *J. Phys. Oceanogr.*, 37, 1077–1091, https://doi.org/10.1175/JPO3035.1.
- Crespo, L. R., M. Belén Rodríguez-Fonseca, I. Polo, N. Keenlyside, and D. Dommenget, 2022: Multidecadal variability of ENSO in a recharge oscillator framework. *Environ. Res. Lett.*, 17, 074008, https://doi.org/10.1088/1748-9326/ac72a3.
- DiNezio, P. N., and C. Deser, 2014: Nonlinear controls on the persistence of La Niña. J. Climate, 27, 7335–7355, https://doi.org/10.1175/JCLI-D-14-00033.1.
- Dommenget, D., and Y. Yu, 2017: The effects of remote SST forcings on ENSO dynamics, variability and diversity. *Climate Dyn.*, 49, 2605–2624, https://doi.org/10.1007/s00382-016-3472-1.
- —, and M. Al-Ansari, 2023: Asymmetries in the ENSO phase space. *Climate Dyn.*, **60**, 2147–2166, https://doi.org/10.1007/ s00382-022-06392-0.
- Fang, X.-H., and M. Mu, 2018: A three-region conceptual model for central Pacific El Niño including zonal advective feedback. J. Climate, 31, 4965–4979, https://doi.org/10.1175/JCLI-D-17-0633.1.
- —, and F. Zheng, 2021: Effect of the air–sea coupled system change on the ENSO evolution from boreal spring. *Climate Dyn.*, 57, 109–120, https://doi.org/10.1007/s00382-021-05697-w.
- —, and N. Chen, 2023: Quantifying the predictability of ENSO complexity using a statistically accurate multiscale stochastic model and information theory. *J. Climate*, 36, 2681–2702, https://doi.org/10.1175/JCLI-D-22-0151.1.
- Fedorov, A. V., 2010: Ocean response to wind variations, warm water volume, and simple models of ENSO in the low-frequency approximation. *J. Climate*, 23, 3855–3873, https://doi.org/10.1175/2010JCLI3044.1.
- Frauen, C., and D. Dommenget, 2012: Influences of the tropical Indian and Atlantic Oceans on the predictability of ENSO. Geophys. Res. Lett., 39, L02706, https://doi.org/10.1029/ 2011GL050520.
- Gadgil, S., P. V. Joseph, and N. V. Joshi, 1984: Ocean–atmosphere coupling over monsoon regions. *Nature*, 312, 141–143, https:// doi.org/10.1038/312141a0.
- Gasparin, F., and D. Roemmich, 2017: The seasonal march of the equatorial Pacific upper-ocean and its El Niño variability. *Prog. Oceanogr.*, 156, 1–16, https://doi.org/10.1016/j.pocean. 2017.05.010.
- Geng, T., W. Cai, and L. Wu, 2020: Two types of ENSO varying in tandem facilitated by nonlinear atmospheric convection. *Geophys. Res. Lett.*, 47, e2020GL088784, https://doi.org/10. 1029/2020GL088784.
- Giese, B. S., and S. Ray, 2011: El Niño variability in simple ocean data assimilation (SODA), 1871–2008. J. Geophys. Res., 116, C02024, https://doi.org/10.1029/2010JC006695.
- Graham, F. S., J. N. Brown, A. T. Wittenberg, and N. J. Holbrook, 2015: Reassessing conceptual models of ENSO. J. Climate, 28, 9121–9142, https://doi.org/10.1175/JCLI-D-14-00812.1.
- Hasegawa, T., T. Horii, and K. Hanawa, 2006: Two different features of discharge of equatorial upper ocean heat content related to El Niño events. *Geophys. Res. Lett.*, 33, L02609, https://doi.org/10.1029/2005GL024832.
- Hayashi, M., F.-F. Jin, and M. F. Stuecker, 2020: Dynamics for El Niño-La Niña asymmetry constrain equatorial-Pacific warming pattern. *Nat. Commun.*, 11, 4230, https://doi.org/10.1038/ s41467-020-17983-y.
- He, J., N. C. Johnson, G. A. Vecchi, B. Kirtman, A. T. Wittenberg, and S. Sturm, 2018: Precipitation sensitivity to local

- variations in tropical sea surface temperature. *J. Climate*, **31**, 9225–9238, https://doi.org/10.1175/JCLI-D-18-0262.1.
- Iwakiri, T., and M. Watanabe, 2022: Multiyear ENSO dynamics as revealed in observations, climate model simulations, and the linear recharge oscillator. *J. Climate*, 35, 7625–7642, https://doi. org/10.1175/JCLI-D-22-0108.1.
- Izumo, T., 2003: The equatorial undercurrent and associated mass and heat exchanges in the tropical Pacific: Variability, links with El Niño-La Niña events. Ph.D. manuscript, Université Paul Sabatier Toulouse III, 239 pp.
- —, 2005: The equatorial undercurrent, meridional overturning circulation, and their roles in mass and heat exchanges during El Niño events in the tropical Pacific Ocean. *Ocean Dyn.*, 55, 110–123, https://doi.org/10.1007/s10236-005-0115-1.
- —, and M. Colin, 2022: Improving and harmonizing El Niño recharge indices. *Geophys. Res. Lett.*, 49, e2022GL101003, https://doi.org/10.1029/2022GL101003.
- —, and Coauthors, 2010: Influence of the state of the Indian Ocean dipole on the following year's El Niño. *Nat. Geosci.*, 3, 168–172, https://doi.org/10.1038/ngeo760.
- —, M. Lengaigne, J. Vialard, J.-J. Luo, T. Yamagata, and G. Madec, 2014: Influence of Indian Ocean dipole and Pacific recharge on following year's El Niño: Interdecadal robustness. *Climate Dyn.*, 42, 291–310, https://doi.org/10.1007/s00382-012-1628-1.
- —, J. Vialard, H. Dayan, M. Lengaigne, and I. Suresh, 2016: A simple estimation of equatorial Pacific response from windstress to untangle Indian Ocean dipole and basin influences on El Niño. Climate Dyn., 46, 2247–2268, https://doi.org/10.1007/s00382-015-2700-4.
- ——, M. Khodri, M. Lengaigne, and I. Suresh, 2018: A subsurface Indian Ocean dipole response to tropical volcanic eruptions. *Geophys. Res. Lett.*, 45, 9150–9159, https://doi.org/10.1029/ 2018GL078515.
- ——, M. Lengaigne, J. Vialard, I. Suresh, and Y. Planton, 2019: On the physical interpretation of the lead relation between warm water volume and the El Niño Southern Oscillation. *Climate Dyn.*, **52**, 2923–2942, https://doi.org/10.1007/s00382-018-4313-1.
- —, J. Vialard, M. Lengaigne, and I. Suresh, 2020: Relevance of relative sea surface temperature for tropical rainfall interannual variability. *Geophys. Res. Lett.*, 47, e2019GL086182, https://doi.org/10.1029/2019GL086182.
- Jin, F.-F., 1997a: An equatorial ocean recharge paradigm for ENSO. Part I: Conceptual model. J. Atmos. Sci., 54, 811–829, https://doi.org/10.1175/1520-0469(1997)054<0811:AEORPF>2.0.CO;2.
- —, 1997b: An equatorial ocean recharge paradigm for ENSO. Part II: A stripped-down coupled model. *J. Atmos. Sci.*, **54**, 830–847, https://doi.org/10.1175/1520-0469(1997)054<0830: AEORPF>2.0.CO:2.
- —, and S.-I. An, 1999: Thermocline and zonal advective feed-backs within the equatorial ocean recharge oscillator model for ENSO. *Geophys. Res. Lett.*, 26, 2989–2992, https://doi.org/10.1029/1999GL002297.
- —, L. Lin, A. Timmermann, and J. Zhao, 2007: Ensemblemean dynamics of the ENSO recharge oscillator under statedependent stochastic forcing. *Geophys. Res. Lett.*, 34, L03807, https://doi.org/10.1029/2006GL027372.
- —, H.-C. Chen, S. Zhao, M. Hayashi, C. Karamperidou, M. F. Stuecker, R. Xie, and L. Geng, 2020: Simple ENSO models. El Niño Southern Oscillation in a Changing Climate, Geophys. Monogr., Vol. 253, Amer. Geophys. Union, 119–151, https://doi.org/10.1002/9781119548164.ch6.

- Johnson, N. C., and S.-P. Xie, 2010: Changes in the sea surface temperature threshold for tropical convection. *Nat. Geosci.*, 3, 842–845, https://doi.org/10.1038/ngeo1008.
- —, and Y. Kosaka, 2016: The impact of eastern equatorial Pacific convection on the diversity of boreal winter El Niño teleconnection patterns. *Climate Dyn.*, 47, 3737–3765, https:// doi.org/10.1007/s00382-016-3039-1.
- Jourdain, N. C., M. Lengaigne, J. Vialard, T. Izumo, and A. Sen Gupta, 2016: Further insights on the influence of the Indian Ocean dipole on the following year's ENSO from observations and CMIP5 models. J. Climate, 29, 637–658, https://doi. org/10.1175/JCLI-D-15-0481.1.
- Keane, A., B. Krauskopf, and C. Postlethwaite, 2016: Investigating irregular behavior in a model for the El Niño Southern Oscillation with positive and negative delayed feedback. SIAM J. Appl. Dyn. Syst., 15, 1656–1689, https://doi.org/10.1137/16M1063605.
- Khodri, M., and Coauthors, 2017: Tropical explosive volcanic eruptions can trigger El Niño by cooling tropical Africa. *Nat. Commun.*, 8, 778, https://doi.org/10.1038/s41467-017-00755-6.
- Kug, J.-S., and I.-S. Kang, 2006: Interactive feedback between ENSO and the Indian Ocean. J. Climate, 19, 1784–1801, https://doi.org/10.1175/JCL13660.1.
- —, F.-F. Jin, and S.-I. An, 2009: Two types of El Niño events: Cold tongue El Niño and warm pool El Niño. *J. Climate*, 22, 1499–1515, https://doi.org/10.1175/2008JCL12624.1.
- —, J. Choi, S.-I. An, F.-F. Jin, and A. T. Wittenberg, 2010: Warm pool and cold tongue El Niño events as simulated by the GFDL 2.1 coupled GCM. *J. Climate*, 23, 1226–1239, https://doi.org/10.1175/2009JCLI3293.1.
- Linz, M., E. Tziperman, and D. G. MacMartin, 2014: Process-based analysis of climate model ENSO simulations: Intermodel consistency and compensating errors. *J. Geophys. Res. Atmos.*, 119, 7396–7409, https://doi.org/10.1002/2013JD021415.
- Lu, B., F.-F. Jin, and H.-L. Ren, 2018: A coupled dynamic index for ENSO periodicity. *J. Climate*, 31, 2361–2376, https://doi. org/10.1175/JCLI-D-17-0466.1.
- Luo, J.-J., R. Zhang, S. K. Behera, Y. Masumoto, F.-F. Jin, R. Lu-kas, and T. Yamagata, 2010: Interaction between El Niño and extreme Indian Ocean dipole. *J. Climate*, 23, 726–742, https://doi.org/10.1175/2009JCLI3104.1.
- McCreary, J. P., Jr., and Z. Yu, 1992: Equatorial dynamics in a 2 and 1/2-layer model. *Prog. Oceanogr.*, 29, 61–132, https://doi.org/10.1016/0079-6611(92)90003-I.
- —, and P. Lu, 1994: Interaction between the subtropical and equatorial ocean circulations: The subtropical cell. *J. Phys. Oceanogr.*, 24, 466–497, https://doi.org/10.1175/1520-0485(1994)024<0466:IBTSAE>2.0.CO;2.
- McPhaden, M. J., 2012: A 21st century shift in the relationship between ENSO SST and warm water volume anomalies. *Geophys. Res. Lett.*, 39, L09706, https://doi.org/10.1029/2012GL051826.
- Meinen, C. S., and M. J. McPhaden, 2000: Observations of warm water volume changes in the equatorial Pacific and their relationship to El Niño and La Niña. *J. Climate*, 13, 3551–3559, https://doi.org/10.1175/1520-0442(2000)013<3551:OOWWVC>2.0.CO;2.
- Menkes, C. E., M. Lengaigne, P. Marchesiello, N. C. Jourdain, E. M. Vincent, J. Lefèvre, F. Chauvin, and J.-F. Royer, 2012: Comparison of tropical cyclogenesis indices on seasonal to interannual timescales. *Climate Dyn.*, 38, 301–321, https://doi. org/10.1007/s00382-011-1126-x.

- Neelin, J. D., D. S. Battisti, A. C. Hirst, F.-F. Jin, Y. Wakata, T. Yamagata, and S. E. Zebiak, 1998: ENSO theory. J. Geophys. Res., 103, 14261–14290, https://doi.org/10.1029/97JC03424.
- Okumura, Y. M., 2019: ENSO diversity from an atmospheric perspective. *Curr. Climate Change Rep.*, **5**, 245–257, https://doi.org/10.1007/s40641-019-00138-7.
- Palanisamy, H., A. Cazenave, T. Delcroix, and B. Meyssignac, 2015: Spatial trend patterns in the Pacific Ocean sea level during the altimetry era: The contribution of thermocline depth change and internal climate variability. *Ocean Dyn.*, 65, 341–356, https://doi.org/10.1007/s10236-014-0805-7.
- Picaut, J., M. Ioualalen, C. Menkes, T. Delcroix, and M. J. McPhaden, 1996: Mechanism of the zonal displacements of the Pacific warm pool: Implications for ENSO. *Science*, 274, 1486–1489, https://doi.org/10.1126/science.274.5292.1486.
- —, F. Masia, and Y. du Penhoat, 1997: An advective-reflective conceptual model for the oscillatory nature of the ENSO. Science, 277, 663–666, https://doi.org/10.1126/science.277.5326.663.
- Planton, Y., J. Vialard, E. Guilyardi, M. Lengaigne, and T. Izumo, 2018: Western Pacific oceanic heat content: A better predictor of La Niña than of El Niño. *Geophys. Res. Lett.*, 45, 9824–9833, https://doi.org/10.1029/2018GL079341.
- Power, S. B., 2011: Simple analytic solutions of the linear delayedaction oscillator equation relevant to ENSO theory. *Theor. Appl. Climatol.*, **104**, 251–259, https://doi.org/10.1007/s00704-010-0339-y.
- Rayner, N. A., D. E. Parker, E. B. Horton, C. K. Folland, L. V. Alexander, D. P. Rowell, E. C. Kent, and A. Kaplan, 2003: Global analyses of sea surface temperature, sea ice, and night marine air temperature since the late nineteenth century. J. Geophys. Res., 108, 4407, https://doi.org/10.1029/2002JD002670.
- Rebert, J. P., J. R. Donguy, G. Eldin, and K. Wyrtki, 1985: Relations between sea level, thermocline depth, heat content, and dynamic height in the tropical Pacific Ocean. *J. Geophys. Res.*, 90, 11719–11725, https://doi.org/10.1029/JC090iC06p11719.
- Ren, H.-L., and F.-F. Jin, 2013: Recharge oscillator mechanisms in two types of ENSO. *J. Climate*, **26**, 6506–6523, https://doi.org/10.1175/JCLI-D-12-00601.1.
- Reynolds, R. W., N. A. Rayner, T. M. Smith, D. C. Stokes, and W. Wang, 2002: An improved in situ and satellite SST analysis for climate. *J. Climate*, **15**, 1609–1625, https://doi.org/10.1175/1520-0442(2002)015<1609:AIISAS>2.0.CO;2.
- Saji, N. H., B. N. Goswami, P. N. Vinayachandran, and T. Yama-gata, 1999: A dipole mode in the tropical Indian Ocean. *Nature*, 401, 360–363, https://doi.org/10.1038/43854.
- Santoso, A., M. J. Mcphaden, and W. Cai, 2017: The defining characteristics of ENSO extremes and the strong 2015/2016 El Niño. Rev. Geophys., 55, 1079–1129, https://doi.org/10. 1002/2017RG000560.
- Shin, N.-Y., J.-S. Kug, M.-F. Stuecker, F.-F. Jin, A. Timmermann, and G. I. Kim, 2022: More frequent central Pacific El Niño and stronger eastern Pacific El Niño in a warmer climate. *npj Climate Atmos. Sci.*, 5, 101, https://doi.org/10.1038/s41612-022-00324-9.
- Srinivas, G., J. Vialard, M. Lengaigne, T. Izumo, and E. Guilyardi, 2022: Relative contributions of sea surface temperature and atmospheric nonlinearities to ENSO asymmetrical rainfall response. J. Climate, 35, 3725–3745, https://doi.org/10.1175/ JCLI-D-21-0257.1.
- Stellema, A., A. Sen Gupta, A. S. Taschetto, and M. Feng, 2022: Pacific equatorial undercurrent: Mean state, sources, and future changes across models. *Front. Climate*, 4, 933091, https://doi.org/10.3389/fclim.2022.933091.

- Stuecker, M. F., A. Timmermann, F.-F. Jin, S. McGregor, and H.-L. Ren, 2013: A combination mode of the annual cycle and the El Niño/Southern Oscillation. *Nat. Geosci.*, 6, 540– 544, https://doi.org/10.1038/ngeo1826.
- Suarez, M. J., and P. S. Schopf, 1988: A delayed action oscillator for ENSO. J. Atmos. Sci., 45, 3283–3287, https://doi.org/10. 1175/1520-0469(1988)045<3283:ADAOFE>2.0.CO;2.
- Sullivan, A., J.-J. Luo, A. C. Hirst, D. Bi, W. Cai, and J. He, 2016: Robust contribution of decadal anomalies to the frequency of central-Pacific El Niño. Sci. Rep., 6, 38540, https://doi.org/10. 1038/srep38540.
- Takahashi, K., A. Montecinos, K. Goubanova, and B. Dewitte, 2011: ENSO regimes: Reinterpreting the canonical and Modoki El Niño. *Geophys. Res. Lett.*, 38, L10704, https://doi.org/ 10.1029/2011GL047364.
- —, C. Karamperidou, and B. Dewitte, 2019: A theoretical model of strong and moderate El Niño regimes. *Climate Dyn.*, **52**, 7477–7493, https://doi.org/10.1007/s00382-018-4100-z.
- Thual, S., and B. Dewitte, 2023: The role of spatial shifting in El Niño/Southern Oscillation complexity. EGU General Assembly 2023, Vienna, Austria, Abstract EGU23-16921.
- —, M. Ayoub, and O. Thual, 2013: An asymptotic expansion for the recharge–discharge model of ENSO. *J. Phys. Oceanogr.*, 43, 1407–1416, https://doi.org/10.1175/JPO-D-12-0161.1.
- Timmermann, A., and Coauthors, 2018: El Niño–Southern Oscillation complexity. *Nature*, 559, 535–545, https://doi.org/10.1038/s41586-018-0252-6.
- Tippett, M. K., S. J. Camargo, and A. H. Sobel, 2011: A Poisson regression index for tropical cyclone genesis and the role of large-scale vorticity in genesis. *J. Climate*, 24, 2335–2357, https://doi.org/10.1175/2010JCLJ3811.1.
- Trenberth, K. E., and D. P. Stepaniak, 2001: Indices of El Niño evolution. *J. Climate*, **14**, 1697–1701, https://doi.org/10.1175/1520-0442(2001)014<1697:LIOENO>2.0.CO;2.
- Tziperman, E., M. A. Cane, and S. E. Zebiak, 1995: Irregularity and locking to the seasonal cycle in an ENSO prediction model as explained by the quasi-periodicity route to chaos. *J. Atmos. Sci.*, 52, 293–306, https://doi.org/10.1175/1520-0469(1995)052<0293:IALTTS>2.0.CO;2.
- van Oldenborgh, G. J., H. Hendon, T. Stockdale, M. L'Heureux, E. C. De Perez, R. Singh, and M. Van Aalst, 2021: Defining El Niño indices in a warming climate. *Environ. Res. Lett.*, **16**, 044003, https://doi.org/10.1088/1748-9326/abe9ed.
- Vecchi, G. A., and B. J. Soden, 2007: Effect of remote sea surface temperature change on tropical cyclone potential intensity. *Nature*, 450, 1066–1070, https://doi.org/10.1038/nature06423.
- Vialard, J., C. Menkes, J.-P. Boulanger, P. Delecluse, E. Guilyardi, M. J. McPhaden, and G. Madec, 2001: A model study of oceanic mechanisms affecting equatorial Pacific sea surface temperature during the 1997–98 El Niño. J. Phys. Oceanogr., 31, 1649–1675, https://doi.org/10.1175/1520-0485(2001)031<1649: AMSOOM>2.0.CO;2.
- Vincent, E. M., M. Lengaigne, C. E. Menkes, N. C. Jourdain, P. Marchesiello, and G. Madec, 2011: Interannual variability of the South Pacific convergence zone and implications for tropical cyclone genesis. *Climate Dyn.*, 36, 1881–1896, https:// doi.org/10.1007/s00382-009-0716-3.
- Wang, C., 2001: A unified oscillator model for the El Niño–Southern Oscillation. J. Climate, 14, 98–115, https://doi.org/10.1175/1520-0442(2001)014<0098:AUOMFT>2.0.CO;2.
- —, and J. Picaut, 2004: Understanding ENSO physics—A review. Earth's Climate: The Ocean–Atmosphere Interaction,

- *Geophys. Monogr.*, Vol. 147, Amer. Geophys. Union, 21–48, https://doi.org/10.1029/147GM02.
- Wang, R., and H.-L. Ren, 2017: The linkage between two ENSO types/modes and the interdecadal changes of ENSO around the year 2000. Atmos. Oceanic Sci. Lett., 10, 168–174, https://doi.org/10.1080/16742834.2016.1258952.
- Williams, I. N., and C. M. Patricola, 2018: Diversity of ENSO events unified by convective threshold sea surface temperature: A nonlinear ENSO index. *Geophys. Res. Lett.*, 45, 9236–9244, https://doi.org/10.1029/2018GL079203.
- Wyrtki, K., 1985: Water displacements in the Pacific and the genesis of El Niño cycles. J. Geophys. Res., 90, 7129–7132, https://doi.org/10.1029/JC090iC04p07129.
- Yu, Y., D. Dommenget, C. Frauen, G. Wang, and S. Wales, 2016: ENSO dynamics and diversity resulting from the recharge oscillator interacting with the slab ocean. *Climate Dyn.*, 46, 1665–1682, https://doi.org/10.1007/s00382-015-2667-1.
- Zeller, M., S. McGregor, and P. Spence, 2019: Hemispheric asymmetry of the Pacific shallow meridional overturning circulation.

- J. Geophys. Res. Oceans, 124, 5765–5786, https://doi.org/10.1029/ 2018JC014840.
- —, E. van Sebille, A. Capotondi, and P. Spence, 2021: Subtropical-tropical pathways of spiciness anomalies and their impact on equatorial Pacific temperature. *Climate Dyn.*, **56**, 1131–1144, https://doi.org/10.1007/s00382-020-05524-8.
- Zhang, W., S. Li, F.-F. Jin, R. Xie, C. Liu, M. F. Stuecker, and A. Xue, 2019: ENSO regime changes responsible for decadal phase relationship variations between ENSO sea surface temperature and warm water volume. *Geophys. Res. Lett.*, 46, 7546–7553, https://doi.org/10.1029/2019GL082943.
- Zhu, X., R. J. Greatbatch, and M. Claus, 2017: Interannual variability of tropical Pacific sea level from 1993 to 2014. J. Geophys. Res. Oceans, 122, 602–616, https://doi.org/10.1002/2016JC012347.
- Zuo, H., M. A. Balmaseda, S. Tietsche, K. Mogensen, and M. Mayer, 2019: The ECMWF operational ensemble reanalysis-analysis system for ocean and sea ice: A description of the system and assessment. *Ocean Sci.*, 15, 779–808, https://doi.org/10.5194/os-15-779-2019.